Agricultural and Forest Meteorology 321 (2022) 108981

Contents lists available at ScienceDirect

Agricultural and Forest Meteorology

journal homepage: www.elsevier.com/locate/agrformet

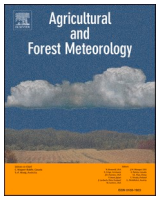

UAS-based high resolution mapping of evapotranspiration in a Mediterranean tree-grass ecosystem

Jake E. Simpson [a], Fenner H. Holman [b], Hector Nieto [c], Tarek S. El-Madany [d], Mirco Migliavacca [d,e], M. Pilar Martin [f], Vicente Burchard-Levine [f], Arnaud Cararra [g], Solveig Blöcher [h], Peter Fiener [i], Jed O. Kaplan [i,j,*]

[a] 86154 Augsburg, Germany
[b] SE15 London, United Kingdom
[c] Institute of Agricultural Sciences (CSIC), Tec4AGRO Group, Serrano, 115b, 28006, Madrid, Spain
[d] Department of Biogeochemical Integration, Max Planck Institute for Biogeochemistry, Jena, Germany
[e] European Commission Joint Research Centre, Via Enrico Fermi 2749, Ispra (VA), Italy
[f] Environmental Remote Sensing and Spectroscopy Laboratory (SpecLab), Spanish National Research Council (CSIC), 28037 Madrid, Spain
[g] Fundación Centro de Estudios Ambientales del Mediterráneo (CEAM), 46980 Valencia, Spain
[h] 86157 Augsburg, Germany
[i] Institute of Geography, Augsburg University, 86159 Augsburg, Germany
[j] Department of Earth Sciences, The University of Hong Kong, Hong Kong SAR, China

ARTICLE INFO

Keywords:
Surface energy budget
Thermal infrared
UAV
Dehesa
Oak savanna
Eddy covariance

ABSTRACT

Understanding the impact of land use and land cover change on surface energy and water budgets is increasingly important in the context of climate change research. Eddy covariance (EC) methods are the gold standard for high temporal resolution measurements of water and energy fluxes, but cannot resolve spatial heterogeneity and are limited in scope to the tower footprint (few hundred meter range). Satellite remote sensing methods have excellent coverage, but lack spatial and temporal resolution. Long-range unmanned aerial systems (UAS) can complement these other methods with high spatial resolution over larger areas. Here we use UAS thermography and multispectral data as inputs to two variants of the Two Source Energy Balance Model to accurately map surface energy and water fluxes over a nutrient manipulation experiment in a managed semi-natural oak savanna from peak growing season to senescence. We use energy flux measurements from 6 EC stations to evaluate the performance of our method and achieve good accuracy (RMSD $\approx$ 60 W m^{-2} for latent heat flux). We use the best performing latent heat estimates to produce very high-resolution evapotranspiration (ET) maps, and investigate the drivers of ET change over the transition to the senescence period. We find that nitrogen and nitrogen plus phosphorus treatments lead to significant increases in ET ($P < 0.001$) for both trees (4 and 6%, respectively) and grass (12 and 9%, respectively) compared to the control. These results highlight that the high sensitivity and spatial and temporal resolution of a UAS system allows the precise estimation of relative water and energy fluxes over heterogeneous vegetation cover.

1. Introduction

Evapotranspiration (ET) is the flux of water and energy from the Earth's land surface to the atmosphere through the combination of evaporation and transpiration. It is the main cause of water loss from terrestrial ecosystems, and an important driver of regional climate (Famiglietti and Wood, 1991). Quantifying ET both temporally and spatially can yield significant benefits to society (Fisher et al., 2017), e.g., by increasing crop yield through precision irrigation (Nocco et al., 2019; Payero et al., 2008), improving freshwater management, especially in areas with limited water (Lu et al., 2019), and reducing uncertainty in weather and climate predictions (Arnault et al., 2016; Fersch et al., 2020; Heinzeller et al., 2018; Liu et al., 2012). For example, accurately capturing ET is fundamental to calculating water use efficiency (WUE), a key metric describing the water usage of plants per unit plant production (Hatfield and Dold, 2019; Ogutu et al., 2021). The

* Corresponding author.
E-mail addresses: jed.kaplan@hku.hk, jed.kaplan@arve-research.com (J.O. Kaplan).

https://doi.org/10.1016/j.agrformet.2022.108981
Received 11 November 2021; Received in revised form 1 March 2022; Accepted 29 April 2022
Available online 8 May 2022

United Nations Sustainable Development Goals (UN-SDGs) identify increasing WUE globally as key to boosting agricultural production and reducing water shortages (Ellison et al., 2017; United Nations, 2015). The United Nations Environment Programme has also emphasized the need for fine-scale measurements of environmental and biophysical variables across farming, pastoral, and forestry systems in order to measure the progress of SGDs into the future (UNEP, 2019). There is, however, a distinct knowledge gap in how different land use strategies affect ET, and thus WUE (Hatfield and Dold, 2019).

High temporal and spatial reference observations are also required to evaluate the performance of low resolution, but wide-reaching, remote sensing data such as the Moderate Resolution Imaging Spectroradiometer (MODIS) global ET products (Kim et al., 2012), as well as to train and test landscape-scale simulations such as regional vegetation and climate models used to predict how both natural and managed ecosystems may interact with a changing climate (Singh et al., 2021; Sylla et al., 2018; Wang et al., 2020). Climate model simulations and low-resolution remote sensing estimates of ET often disagree, perhaps owing to sub-pixel heterogeneity in biophysical parameters (Burchard-Levine et al., 2021), and mismatch between the spatial scales of both products (Chao et al., 2021; Sullivan et al., 2019).

To measure ET with high accuracy, established methods include using lysimeters (Gebler et al., 2015; Perez-Priego et al., 2017) and micrometeorology using eddy covariance (EC, Foken et al., 2012). While lysimeters can precisely measure soil water loss directly, they disturb the surface during installation, must be installed in large numbers to capture vertical and horizontal variability, and require manual intervention, so are difficult to deploy at scale. In contrast, EC provides a spatially integrated view of ecosystem-scale fluxes by measuring surface energy fluxes in combination with meteorological variables using instruments positioned above the vegetation canopy.

An EC station measures fluxes over a footprint that represents the area upwind of the station that is contributing to the station's flux measurements, and depending on the tower height, can reach hundreds of meters (Barcza et al., 2009). Footprints are usually calculated over a 30 min period so that both small and large scale eddies are captured (Heidbach et al., 2017; Kljun et al., 2015). Footprint delineation depends on a variety of atmospheric boundary layer conditions including windspeed and direction, atmospheric stability, turbulence, and surface characteristics such as surface roughness (Heidbach et al., 2017; Kljun et al., 2015; Rebmann et al., 2018). The accuracy of the estimated footprint depends on parameterization of the footprint model using data collected by instruments at the station. To limit possible sources of measurement error, and keep surface roughness constant, EC stations are usually located above the canopy of a homogeneous vegetation type, e.g., grass, forest, crop (Kljun et al., 2015).

The disadvantage of the EC approach is that single stations cannot disentangle the individual flux signals in heterogenous ecosystems or differentiate among the vertical components of a mixed canopy (Knauer et al., 2018). The same issue is relevant to investigating land use practices on ET, whereby a single EC station would be required per land use category, e.g., fertilizer treatment or irrigation type, therefore the EC station approach alone can be costly and/or impractical when investigating different drivers of ET in field-scale manipulation experiments (Barcza et al., 2009).

To overcome some of the limitations of lysimeters and EC, remote sensing is increasingly being used to estimate ET. Spaceborne and airborne thermography can be used to estimate land surface temperature (*LST*) and, combined with meteorological and plant structural data, the surface energy budget can be calculated. Models are used to estimate net radiation (*Rn*), sensible (*H*), and ground (*G*) heat fluxes, and the budget residual is then attributed to the latent heat flux (*LE*)

$$LE = Rn - H - G, \quad (1)$$

(Burchard-Levine et al., 2021; Guzinski and Nieto, 2019; Norman et al., 1995). On the basis of this *LE* estimate, evapotranspiration (*ET*) can be calculated.

Accurately mapping ET through remote sensing is challenging, however, because ET is sensitive to a range of factors. Deriving *LST* from thermal imagery relies on accurate estimates of target surface emissivity and atmospheric transmittance, which can cause significant errors if not properly characterized (Heinemann et al., 2020; Schmugge et al., 2002). If the ground sampling distance (pixel size) is too large, pixels that represent a mix of LST and canopy temperature lead to greater errors (Burchard-Levine et al., 2021; Kustas et al., 2004; Susan Morana et al., 1997). Furthermore, meteorological conditions such as windspeed, water availability (Allen et al., 1998; Feng et al., 2020), plant structure including canopy height, leaf area index, leaf shape, albedo, rooting depth (Gates and Hanks, 2015), and soil physical properties (Ekern et al., 2015) all contribute to uncertainty in ET estimates. These factors can be highly variable both spatially and temporally over small scales, e.g., within a single field over the course of day. Nevertheless, the promise of remote sensing is the possibility of generating spatially resolved maps of ET at field (and larger) scale at relatively low cost, and so it is a focus of current research.

Spaceborne thermal imaging sensors present opportunities for mapping ET over very large spatial scales at moderate resolution. While thermal sensors on satellites are typically lower resolution than multispectral imagers, data mining sharpener (DMS) approaches have been used to enhance moderate resolution LST products, e.g., 100–1000 m for the Landsat 8 and Sentinel 3 satellites, to the same resolution as multispectral imagery from co-located sensors (Guzinski and Nieto, 2019). This approach has been successfully applied to map LST at 20 m resolution, which may work well under largely homogenous forests or agricultural landscapes, but is still too coarse for differentiating between different vegetation types in many heterogenous natural and semi-natural ecosystems such as agroforestry, savannas, and shrublands (Burchard-Levine et al., 2021). Furthermore, spaceborne sensors cannot collect LST data under cloudy conditions. Airborne surveys overcome many of the drawbacks of spaceborne sensors, but can be prohibitively expensive and logistically difficult if using piloted aircraft.

Unmanned aerial systems (UAS) have the potential to bridge the temporal and spatial scale gap between EC stations and satellite remote sensing (Simpson et al., 2021) and recent development in both aircraft and sensor technology have led to a wide range of applications to estimate ET with UAS (e.g., Mokhtari et al., 2021; Nassar et al., 2022, 2021, 2020; Nieto et al., 2019; Niu et al., 2020, 2021; Ortega-Farías et al., 2016). Using a UAS can be advantageous because multiple surveys can be conducted per day (temporal resolution: EC > UAS > Satellites), and with a fixed-wing UAS the survey area can be hundreds of hectares in one flight (spatial coverage: Satellite > UAS > EC station) (Torres-Rua, 2017). Furthermore, the ground sampling distance can be sub-meter because thermal infrared sensors are flown at low altitudes on the UAS (spatial resolution: UAS > EC station > satellite). This combination of high spatial and temporal resolutions and medium spatial coverage make the UAS a good candidate for applications such as precision agriculture (Niu et al., 2020), and mapping water stress and ET in ecosystems with mixed vegetation (Nouri et al., 2015; Park, 2018). Furthermore, the UAS approach may be able to detect and estimate sub-site scale variability in ET so that the effects of different drivers, e.g. land use practice differences such as crop type or irrigation scheme, can be measured (Park et al., 2017). This may be particularly pertinent in water-limited, highly fragmented landscapes such as Sub-Saharan Africa where smallholder farms can adopt multiple land use practices in a relatively small plot (Kuivanen et al., 2016; Lowder et al., 2016).

UAS remote sensing does have some limitations, foremost that this method is not a direct measurement of ET, but based on an energy balance model driven by measurements of temperature and vegetation structure. Furthermore, UAS based ET measurements are sensitive to cloud cover, windspeed, precipitation, and temperature, and cannot approach the temporal resolution of EC-based estimates (Mauder et al., 2020). Miniaturized cameras may not have the radiometric quality of

larger, heavier sensors (Burchard-Levine et al., 2022; Kelly et al., 2019). UAS missions are generally limited to line-of-sight flights, flying is restricted in some areas, and the equipment can be expensive.

Nevertheless, the many outstanding questions regarding the role of ET in local, regional and global hydrological systems warrant a range of approaches towards measuring ET over different spatial extents and with different resolution. Fisher et al. (2017) highlight some of these knowledge gaps and identify a need for ET maps with high accuracy, and high temporal and spatial resolution, that cover large areas and over long periods to address these research questions. Here, UAS ET mapping may provide additional spatial and temporal information as a complement to both EC station and satellite remote sensing methods, enabling land users and researchers to manage and monitor vegetation and water resources more efficiently (Niu et al., 2020).

The goal of this study was to establish a protocol for UAS-based ET mapping in complex, heterogenous natural or semi-natural ecosystems that is accurate, able to resolve differences at individual plant scale, and inexpensive to deploy over km^2-scale and larger areas. With this protocol established, we performed a case study, highlighting the UAS' capability to map ET at very fine spatial resolution. We demonstrate the potential of the system to understand how plant-plant interactions, topography, and nutrient treatments affect ET at field scale.

2. Methods

Development of the methodology for UAS-based ET mapping had three main components:

1 Estimate radiometric surface temperature based on thermal images captured with a UAS.
2 Use these surface temperatures, along with plant physical properties estimated from UAS photogrammetry and multispectral images, to drive the Two Source Energy Balance Model (TSEB) and calculate energy and water fluxes.
3 Assess the accuracy of mapped ET based on independent measurements of ET from eddy covariance.

To develop this method, we worked at a field site that is extensively instrumented for micrometeorological observations and where field trials with different nutrient manipulations are underway.

2.1. Study area

Here we studied a tree-grass ecosystem (*dehesa*) typical for central Iberia at Majadas de Tiétar, Caceres, Spain (5.776 °W, 39.939 °N, ca. 265 m above sea level). Vegetation cover at the field site is characteristic of the region and consists of two main strata: an open tree canopy of Holm Oak (*Quercus ilex*) with a tree density around 20–25 stems ha^{-1}, and a herbaceous understory of annual grasses, forbs, and legumes (El-Madany et al., 2018). Typical leaf area index values range between 1.5–2.0 m^2m^{-2} for individual trees, and 0.5–2.5 m^2m^{-2} (Bogdanovich et al., 2021) in the spatially and phenologically heterogeneous herbaceous layer (Migliavacca et al., 2017). We performed a single measurement campaign between 5 and 21 May 2021, which corresponds to the end of annual peak productivity, and the beginning of the dry-down period in the ecosystem (Luo et al., 2018). The principal land use at the site is low-intensity cattle pasture during the winter and spring months (Burchard-Levine et al., 2019).

The Majadas site is also used for a long-term nutrient manipulation experiment with three areas receiving different treatments: one area with additional nitrogen (FLUXNET site code ES-LM1), one area with combined addition of nitrogen and phosphorus fertilizer (ES-LM2), and a control area with no additional fertilizer input (ES-LMa). For details of the effect of fertilization on water use efficiency see El-Madany et al. (2018) and on productivity and phenology Luo et al. (2020).

2.2. Eddy covariance station reference datasets

Within each nutrient treatment area there are two eddy covariance stations capturing meteorological and surface energy balance data, with one measurement point each at grass- and tree-canopy level (1.6 and 15 m above ground level respectively). The three sites are separated by at least 450 m, meaning their flux footprints do not normally overlap under prevailing wind directions (Fig. 1).

Instruments on the 15 m towers provide both meteorological/irradiance and energy data for model inputs and UAS-flux estimate comparisons respectively (Table 1 for details). Both are integrated over 30 min periods. Turbulent fluxes of momentum, H and water vapor (H_2O Flux, LE, ET) were calculated from 3D-measurements of the vertical and horizontal wind components (R3–50 Gill Instruments, Lymington, GB) with an infra-red gas analyzer (LI7200 Licor Bioscience Lincoln, USA) to measure CO_2 and H_2O concentrations. Raw data were collected at 20 Hz using EddySoft (Kolle and Rebmann, 2009). Fluxes were subsequently calculated using EddyPro v. 6.2.0. In short, raw data were despiked, and coordinate rotation was performed using the planar fit method. Time lags between CO_2 concentrations and vertical wind speed (w) were lag-corrected by maximizing the cross-correlation in predefined windows. For H_2O the lag-correction was performed based on bins of relative humidity. High and low frequency corrections were performed following Moncrieff et al. (2004) and Moncrieff et al. (1997). Quality control was performed following the 0–1–2 scheme of Mauder and Foken (2011), where 0 represents highest and 2 lowest quality measurements.

Footprints were estimated using the methodology outlined in Kljun et al. (2015). The datasets were rasterized at 1 m resolution and rotated −90° to ensure correct orientation. Footprints were processed in R (R Core Team, 2020) using the FFP function v 1.41 (Kljun et al., 2015) according to the corresponding flight survey area and time.

EC station-derived fluxes and the radiative fluxes often yield in an imbalance where the energy balance is not fully closed (for full details, see Mauder et al., 2020, 2018). Contrary to the EC-method for measuring fluxes, the UAS flux estimation method forces energy balance closure by adding any residual imbalance to LE. We perform the same closure method in the EC station data, as recommended by Burchard-Levine et al. (2021) who compared EC-measured fluxes with remote sensing estimates at this site.

2.3. Unmanned aerial system data collection and processing

The airborne sensor used in this study was the Micasense Altum (Micasense Inc., Seattle, WA, USA), an integrated 6-band multispectral and thermal infrared sensor (Blue, Green, Red, Red-Edge, Near- Infrared and Longwave Infrared). The sensor was mounted onboard a Quantum Systems Trinity F90+ (Quantum-Systems GmbH, Gilching, Germany) fixed-wing vertical take-off and landing unmanned aerial vehicle. A full description of the UAS can be found in Simpson et al. (2021).

Flight survey areas were planned to cover the maximum extents of each EC station footprint, and were adapted according to the wind direction and strength, i.e., in stronger winds the survey area was widened in the upwind directed to ensure the EC footprint area would be captured in the survey. Flight parameters were maintained for all flights: altitude of 120 m (Above Ground Level), air speed of 17 m s^{-1}, and forward and sideward image overlap were set at 76% and 80%, respectively. The Altum was acclimatized (powered on) for 30 min before flights after rest periods (Kelly et al., 2019). Multispectral images of the Altum calibration panel were collected before and after each flight. Flight timings and survey areas are detailed in Table 2. Meteorological and irradiance data for each flight are reported in Fig. 2. The data collection period corresponds with the transition between spring and summer, when many of the grasses and forbs in the understory start to senesce. This survey window was thus optimally timed, capturing the seasonal peak of biomass and photosynthesis, and the transition to

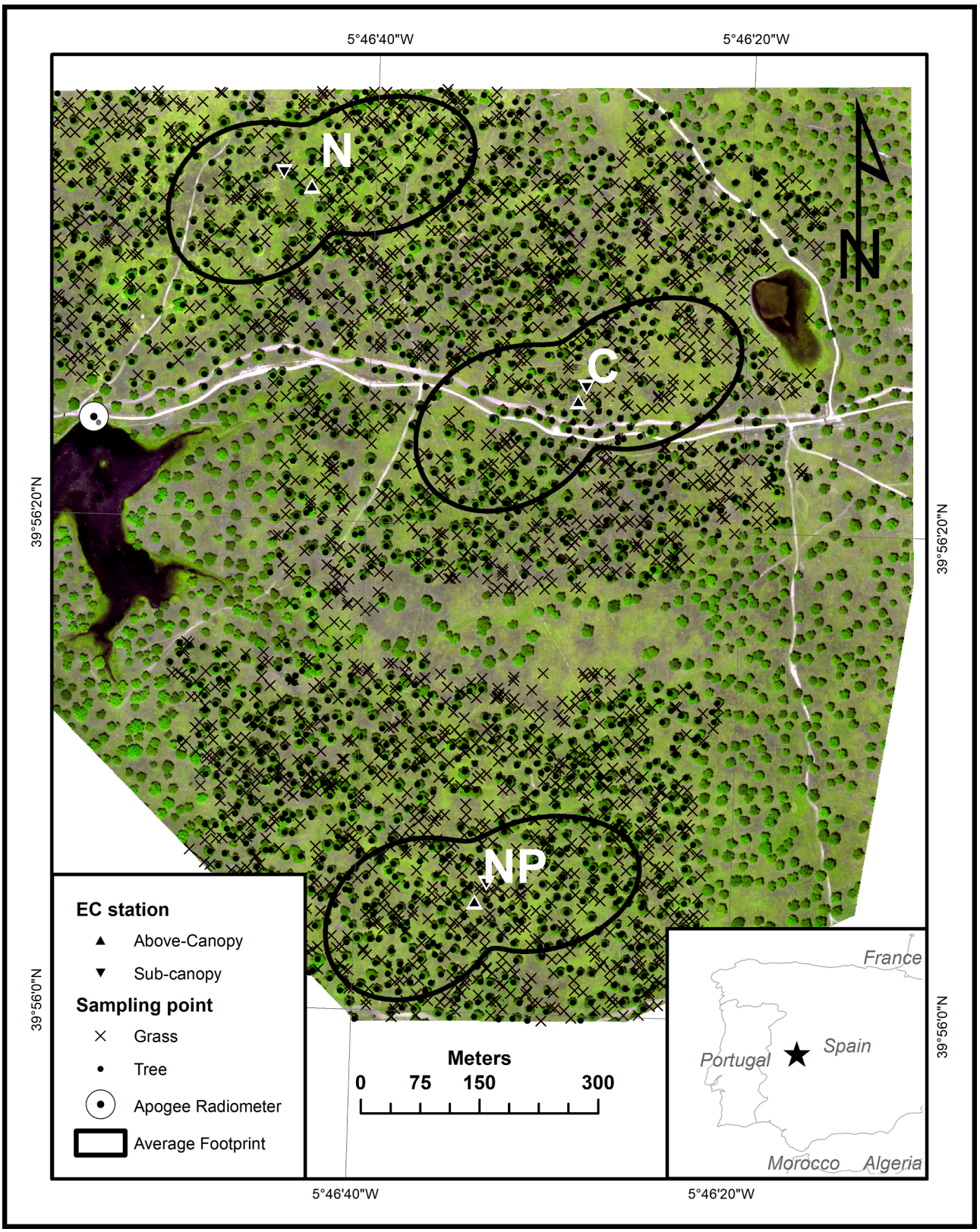

Fig. 1. Majadas Field Site plan showing the location and maximum footprints of the three above-tree canopy and three sub-tree canopy Eddy Covariance towers, where *N* = Nitrogen-added treatment site, C = Control fertilizer treatment site, and NP = Nitrogen-Phosphorous-added treatment site. Sampling points for spatial and temporal analyses are marked for tree (●) and grass (×) locations; note that grass sampling points are excluded around tracks. The Apogee ground control radiometer is also marked (black dot, white circle). The background image is a multispectral false-color composite orthomosaic of the whole survey area from Altum imagery collected at solar noon, 20/05/2021, where the bands are *R* = NIR, *G* = Red-edge, *B* = Red. Projected Coordinate System = WGS84 UTM 30 N. (For interpretation of the references to color in this figure legend, the reader is referred to the web version of this article.)

Table 1
Details of the Eddy Covariance towers used in this study. Towers are named based on the fertilizer treatment zone within which they are located (C = Control, *N* = Nitrogen-added, NP = Nitrogen-Phosphorous-added), and where the tower instruments are positioned above-tree canopy or below-tree canopy (-sub). Tower heights are measured in meters above ground.

Name	Elevation (m ASL)	Location (Degrees)	Fertilizer treatment	Tower height (m)
C	318	39.9403, −5.7746	Control	15
C-sub	317	39.9405, −5.7745	Control	1.6
N	317	39.9427, −5.7786	Nitrogen	15
N-sub	318	39.9428, −5.7791	Nitrogen	1.6
NP	321	39.9360, −5.7759	Nitrogen & Phosphorus	15
NP-sub	321	39.9428, −5.7791	Nitrogen & Phosphorus	1.6

Table 2
Details of flight take-off times, image counts, and areas surveyed within this study. Survey areas refer to the different fertilizer treatment sites, where *N* = Nitrogen-added, C = Control, and NP = Nitrogen-Phosphorous-added. Survey area W refers to a single flight survey inclusive of all three treatment sites and Eddy Covariance towers.

Date	Time	Image count	Survey areas
05/05/2021	07:30	1152	N, C, NP
	11:30	1093	N, C, NP
11/05/2021	07:30	1712	N, C, NP
	10:20	475	N
	12:45	1567	N, C, NP
	16:25	1536	N, C, NP
14/05/2021	07:30	1662	N, C, NP
	11:30	310	N
	12:30	1336	N, C, NP
	14:00	1604	N, C, NP
15/05/2021	07:20	1605	N, C, NP
	10:15	1483	N, C, NP
17/05/2021	07:10	1785	N, C, NP
	09:50	1542	N, C, NP
	11:30	1595	N, C, NP
	12:50	1748	N, C, NP
	14:30	1744	N, C, NP
	16:20	1588	N, C, NP
19/05/2021	07:10	1854	N, C, NP
	09:50	1799	N, C, NP
	11:50	536	N
	12:35	1761	N, C, NP
	14:25	1733	N, C, NP
	15:50	1745	N, C, NP
20/05/2021	11:30	1800	N, C, NP
	13:00	1787	N, C, NP
	14:20	2640	W

full-summer senescence in the grassland canopy. During this period, we aimed to capture ET variability brought about by this rapid phenological change (Luo et al., 2020). We demonstrate this effect in Fig. 3, which shows the change in NDVI from the first survey day (05/05/2021) to the last (20/05/2021).

Raw Altum image trigger locations and orientations were calculated using the Post-Processing Kinematics (PPK) method which uses iBase base-station data to perform offset correction to the "rover" position data. Agisoft Metashape (St. Petersburg, Russia) software was used to apply vignetting, dark pixel and radiometric correction for each image, and to create two orthomosaics per survey area (at the native resolutions of the multispectral and longwave infrared bands, 0.05 and 0.82 m respectively). A single point cloud was generated from an Altum survey of the entire site performed at solar noon (around 14:00 local time) to reduce the effects of tree shadows on point accuracy.

2.4. Energy flux mapping

2.4.1. Two source energy balance (TSEB) and dual time difference (DTD) models

TSEB was developed by Norman et al. (1995) and is an established model for producing spatially explicit flux estimates over different vegetation types and at different scales (Alhassan and Jin, 2020; Bellvert et al., 2021; Burchard-Levine et al., 2020; Guzinski and Nieto, 2019; Hoffmann et al., 2016; Simpson et al., 2021). It estimates LE as the residual of the energy balance by separating the energy exchange between vegetation and soil sources, using the radiometric surface temperature as the main boundary condition. Detailed explanations of the mechanics behind TSEB can be found in the literature (Burchard-Levine et al., 2021; Niu et al., 2020; Norman et al., 1995). We used the open-source Python implementation of TSEB (Nieto et al., 2021) to perform pixel-based simulations to derive net radiation (*Rn*), sensible- (*H*), latent- (*LE*) and ground- (*G*) heat fluxes from a radiometric surface temperature, canopy height model, and green fraction rasters from UAS data, as well as a suite of meteorological and irradiation forcing data (for a summary, see Table 4 in Simpson et al., 2021). In this study we also used the TSEB Dual Time Difference model, which used a radiometric surface temperature layer taken up to 90 min after dawn when canopy and soil sensible heat fluxes are close to zero (Norman et al., 2000). Previous work has shown that this correction improved *H* estimations, and as a result, reduced biases in other fluxes (Brenner et al., 2018; Nieto et al., 2019; Simpson et al., 2021).

However, one of the challenges of TSEB is that it is more sensitive to errors in absolute LST retrieval compared to contextual approaches such as METRIC (Niu et al., 2020), which may not need highly accurate LST retrievals/calibrations (which may be a more important issue with UAV-based sensors). For that reason, the Dual-Temperature Difference (DTD) was developed by (Norman et al., 2000) in order to take advantage of the relative temperature increase in the morning. DTD therefore uses two thermal infrared measurements, one before sunrise and a second one before noon, which in principle minimize potential systematic errors associated to the uncertainty in LST retrieval. Detailed descriptions of the equations and workflows for both TSEB-PT and DTD are contained in recent literature (Nieto et al., 2019; Simpson et al., 2021). Full source code for TSEB is available at Nieto et al. (2021, https://doi.org/10.5281/zenodo.4761984). For further of evaluation of other UAS-based ET models, see (Niu et al., 2020;).

2.4.2. Land surface temperature estimation

The Altum's longwave infrared band retrieval was converted to radiometric land surface temperature using three different methods. The default method involves converting digital number (*DN*) to temperature (K) using

$$T_{RAW} = 0.001DN, \quad (2)$$

where T_{RAW} is radiometric surface temperature (brightness temperature). The second method uses

$$T_{EMP} = 50.2 + 0.00837DN \quad (3)$$

where T_{EMP} is the radiometric surface temperature determined with an empirical relationship where the relationship between *DN* and brightness temperature is established using reference canopy temperature data collected using a high-accuracy infrared radiometer (Section 3.1, Simpson et al., 2021). It should be noted that we used the same sensor as in Simpson et al. (2021), and so this method may not be applicable to other Altum units, however the method is replicable.

Thirdly we employed the methodology from Heinemann et al. (2020) to correct for errors borne from variability in target surface emissivity and atmospheric transmission using

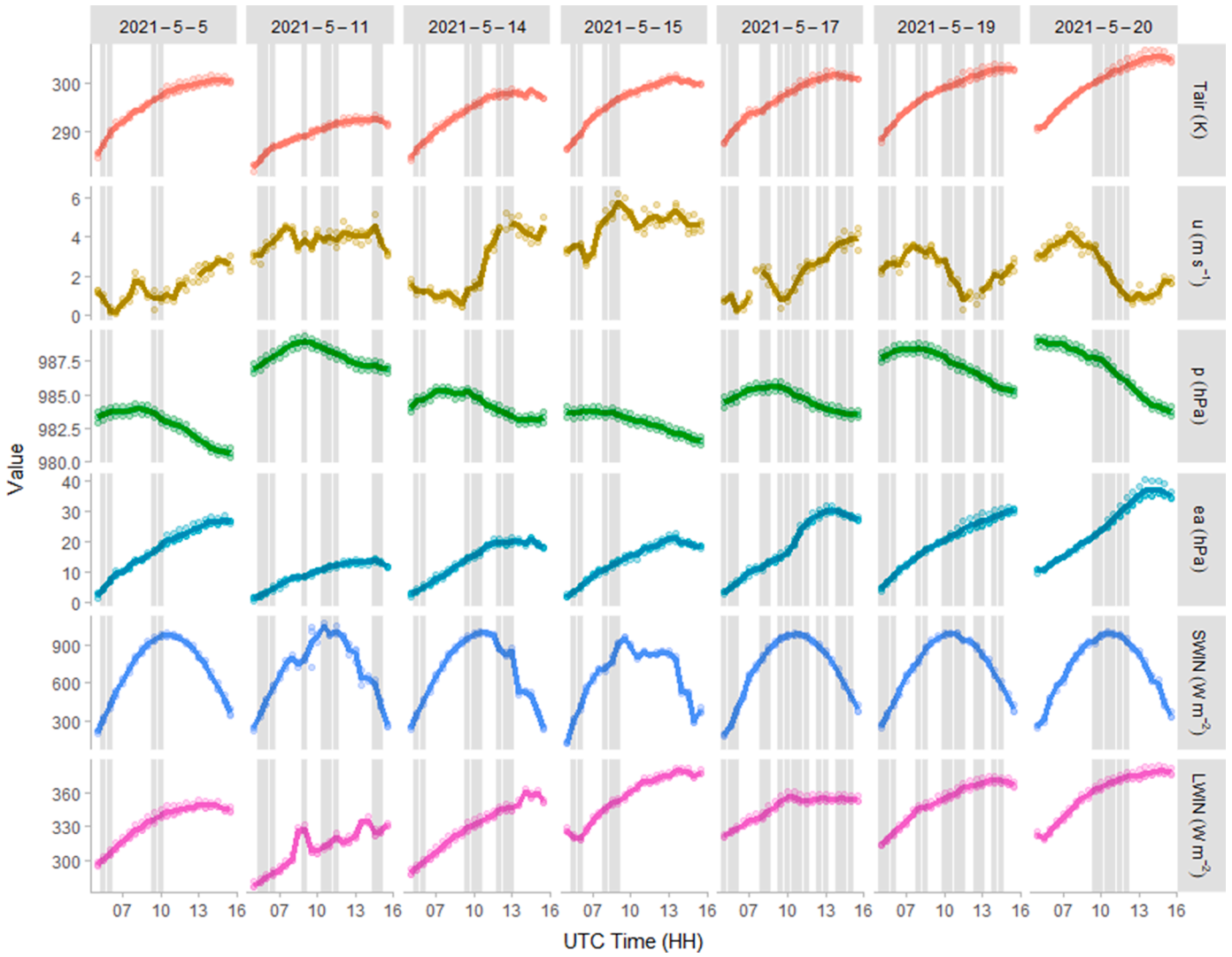

Fig. 2. Meteorological and irradiance data measured over the study period at the three 15 m (Above-tree canopy) Eddy Covariance towers centered in control (C), Nitrogen-added (N), and Nitrogen-Phosphorous-added (NP) fertilizer treatment sites. Individual measurements are plotted as points, means of measurements from all 3 towers are bold lines. Measured parameters are: air temperature (T_{air}), wind speed (u), air pressure (p) water vapor pressure above tree canopy (ea), incoming shortwave radiation (SWIN), and incoming longwave radiation (LWIN). gray vertical bars indicate UAS survey flight periods.

$$T_{LST} = \left[\frac{BT_{sens}^4 - (1-\epsilon)\tau T_{bkg}^4 - (1-\tau)T_{air}^4}{\epsilon\tau}\right]^{1/4} \quad (4)$$

where T_{LST} is the emissivity and transmittance corrected land surface temperature, BT_{sens} is the at-sensor "brightness temperature" (equivalent to T_{raw} in this study) and T_{air} is air temperature (both in K), ε is emissivity and τ is transmittance (ranging 0–1, unitless). T_{air} was measured at the EC stations, whereas T_{bkg} was measured using a PCE-889B Pyrometer (PCE Deutschland GmbH, Meschede, Germany) (set to $\varepsilon = 1$, reported accuracy of 1 K) aimed at a crumpled sheet of aluminum foil at the beginning, midpoint and end of each flight.

Emissivity maps were calculated on a per-pixel basis for grass areas only using an established method (Heinemann et al., 2020). Where pure grass or pure soil pixels have known emissivity values and represent maximum and minimum values respectively, this method calculates emissivity of mixed pixels based on the proportion of the pixel covered by green vegetation/soil.

Our NDVI maps were created from Altum Near Infrared and Red bands at 0.82 m ground sampling distance. NDVI thresholds for pure soil and grass were derived from the midday flight on 05/05/2021 when the grass was its greenest, using the lowest (5th) and highest (99th) percentile NDVI values in the scene to represent pure soil and grass pixels respectively. The resultant thresholds were 0.048 and 0.677 for $NDVI_{soil}$ and $NDVI_{grass}$, respectively. We applied a known emissivity value of 0.985 from Rubio et al. (1997) to the trees on site. Emissivity and transmittance estimates for soil, grass, and trees used as inputs for Eq. (4) were calculated based on Heinemann et al. (2020).

We collected relative humidity and air temperature data from a Kestrel Drop D3 Environmental Data Logger (Kestrel Instruments, Boothwith, PA, USA), mounted in the payload sensor bay of the UAS to derive atmospheric water vapor content, at a fixed distance of 120 m that corresponds to the UAS flight altitude. Before outputting all radiometric surface temperature layers, we applied a shadow mask, calculated by using the 10th percentile values from the near infrared band which is particularly sensitive to shadows and vegetation (Rufenacht et al., 2014).

To assess the performance of each method described above for calculating radiometric surface temperature (T_{RAW}, T_{EMP}, T_{LST}) from the UAS, we installed an SI-220 Apogee Infrared Radiometer (Apogee Instruments, Inc, Logan, UT, USA, wavelengths 8–14 mm corresponding the Altum's longwave infrared band, reported accuracy of 0.1 K), mounted on a tripod and angled 45° at the surface of a small lake

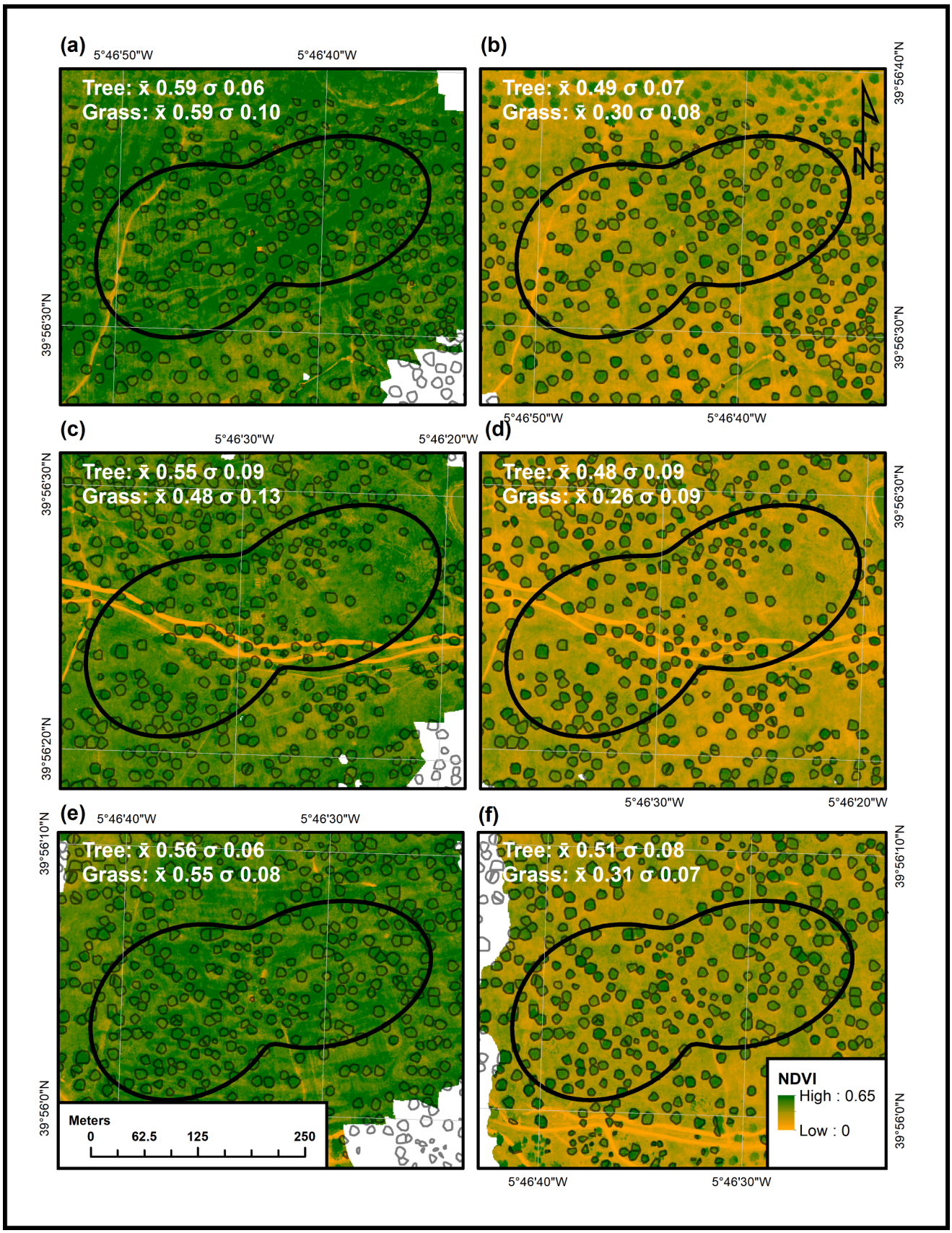

Fig. 3. Variations in Normalized Difference Vegetation Index (NDVI) between 05/05/02021 (a, c, e) and 20/05/2021 (b,d,f) at the Nitrogen-added (N) (a, b), Control (C) (c, d), and Nitrogen-Phosphorous-added (NP) (e, f) fertilizer treatment sites. The thick black polygons denote long-term footprint climatology areas, and gray polygons delineate tree crowns. Mean ($\bar{x}$) and standard deviation (1σ) NDVI statistics are reported in each panel for both canopy layers (Tree and Grass). Projected Coordinate System = WGS84 UTM 30 N.

Table 3
Summary of the statistical tests used to examine the spatial and temporal drivers of Evapotranspiration (ET) variability at the Majadas field site, using UAS imagery derived data. Here random variables are marked with (*). The Explanatory Variables Tested column describes model inputs but does not indicate the final variables used in the models. GAM stands for Generalised Additive Model, GLMM stands for Generalised Linear Mixed Model. In Data Subset, *N* = Nitrogen-added, C = Control, and NP = Nitrogen-Phosphorous-added fertilizer treatment sites.

Model Number	Objective tested	Dataset subset	Explanatory variables tested	N	Model used
1	Time of Day, Vegetation Type	Only data with no fertilizer treatment (O)	Date, Time, Vegetation type	29,760	GAM
2	Date, Elevation, Vegetation	Only data from midday (11:30–13:00) Only data with no fertilizer treatment (O)	Date, Elevation, Time*, Vegetation Type	11,106	GLMM
3	Fertilizer Treatment	Only data from N, C, NP areas Only data from midday (11:30–13:00)	Date*, Elevation, Time*, Fertilizer Treatment, Vegetation Type	5057	GLMM
4	Tree Crown Area, Tree Height	Only data from Trees Only data from midday (11:30–13:00) Only data with no Fertilizer Treatment (O)	Date*, Elevation, Time*, Tree Height, Crown Area	6207	GLMM

Table. 4
Error statistics of UAS-derived energy fluxes for the best-performing DTD-T_{EMP} (Dual Time Difference, Empirical Temperature) model compared to Eddy Covariance tower measurements (n = 2094). For the complete comparison of all surface temperature and Latent heat flux models, see Table S1.

Flux	RMSD (W m^{-2})	Bias	Standard deviation
Ground Heat Flux (G)	25.45	16.61	19.39
Sensible Heat Flux (H)	80.83	−57.64	56.99
Latent Heat Flux (LE)	60.23	9.13	59.87
Net Radiation (Rn)	46.75	−30.76	35.41

(Fig. 1). Data were collected every 20 s. Apogee water surface temperature values were averaged according to the overpass time of the UAS, and thus served as reference values.

2.4.3. Other TSEB inputs

A canopy height model was created from a point cloud output from Agisoft Metashape produced from the data collected during the site-wide survey at solar noon (14:00 CEST) on 20/05/2021. We first processed the point cloud in CloudCompare (Girardeau-Montaut, 2021); decimated the data using random sampling, manually subset to remove visible outliers, then cleaned using Statistical Outlier Removal (SOR) and noise filters. We then used the lidR package in R (Roussel and Auty, 2021) for the remaining steps: 1) classify ground points using the Progressive Morphological Filter, 2) filter ground points, 3) classify noise (SOR), 4) filter ground points again, 5) create digital terrain model (DTM) using k-nearest neighbor approach with an inverse distance weighting in "grid_terrain", 5) normalize height of non-ground and non-noise points against the DTM, 6) set all return number values to 1, 7) use "grid_canopy" to convert normalized points to a pit-free canopy height model. As the Structure-from-Motion approach is not able to capture sub-canopy or grass structure well, we assumed a fixed height value of 0.25 m for the grass, based on the average of ~25 observations made in the field using a ruler. We also removed intermediate CHM values between the grass/tree layers (0.30–4 m) in order to remove mixed pixels in the CHM layer, but also to produce separate grass and tree processing masks. The site-wide CHM, grass and tree masks were then cropped and resampled to fit the radiometric surface temperature layers from each UAS survey.

Green fraction (GF) refers to the proportion of the canopy covered in green vegetation. Daily GF was calculated using the multispectral data from the survey flights closest to solar noon. We derived GF per 0.82 m pixel (LWIR native resolution), using fCover from RStoolbox (Leutner et al., 2019) calculating the proportion of each 0.82 cm pixel covered by 0.05 m pixels of NDVI values above a set threshold (0.25). This value was appropriate because 0.05 m pixels are rarely mixed. GF layers were cropped and resampled to fit each survey area radiometric temperate layer. For DTD processing, it was necessary to crop and resample all raster input data to fit the early morning flight.

Leaf Area Index (LAI) data were taken from field surveys of both tree and grass vegetation strata. Tree LAI were sampled indirectly using an LAI-2200 plant canopy analyzer (LI-COR, Lincoln NB, USA,). A total of 6 trees were measured individually, with LAI ranging between 2.01 and 3.40 m^2 m^{-2} (mean: 2.71 m^2 m^{-2}). Grass LAI measurements were collected over 22 plots (25 m x 25 m) randomly allocated over the CT, NT and NPT tower footprints. At each plot, two samples (total of 44 samples) were acquired through destructive sampling and leaf scanning (Melendo-Vega et al., 2018; Mendiguren et al., 2015). We calculated means from both tree and grass surveys, and applied them as single values to the appropriate processing mask (2.40 and 1.95 m^2 m^{-2} respectively). Meteorological and irradiance forcing data were taken from the EC stations that correspond with the flight survey time and area.

2.4.4. TSEB and DTD model application

We applied the TSEB and DTD models using pyTSEB (Nieto et al., 2021), which allows the user to run TSEB based on a configuration file that defines model parameters and variable locations. This enabled us to create TSEB/DTD outputs for each survey area (N, C, NP), date, time, radiometric surface temperature (T_{RAW}, T_{EMP}, T_{LST}) and each vegetation type (grass and tree).

2.4.5. EC station-UAS flux comparison

Within each flight, the UAS surveyed all six EC station footprints: in each fertilizer treatment area (survey area) EC stations mounted on tall and small towers capture above canopy and sub-canopy fluxes respectively. We extracted sub-canopy fluxes from the grass-only TSEB/DTD outputs using the sub-canopy EC station footprint areas derived in Section 2.2.2, and above-canopy fluxes were extracted from tree and grass TSEB/DTD outputs, using the tall tower footprints. Pixel values for *Rn, H, LE* and *G* were then averaged within each footprint, and compared to the EC station estimate with corresponding time and location. All EC station flux estimates with quality flags more than zero were omitted from comparisons. To ensure comparability between TSEB and DTD estimates, we omitted the early morning flux comparisons from both datasets, as the energy fluxes are low at this time, and thus may artificially inflate performance statistics.

2.4.6. Spatially distributed evapotranspiration estimates

Each EC station estimates ET with the units g m^{-2} s^{-1}. Instantaneous water fluxes can also be derived from latent heat flux (*LE*) layer from TSEB/DTD using the following equations,

$$\lambda = (2.501 - 0.00237T_{air}) \times 10^6 \quad (5)$$

and

$$ET = LE\frac{10^3}{\lambda}, \quad (6)$$

where λ is the latent heat of vaporization (J kg^{-1}), T_{air} is air temperature (°C), ET is evapotranspiration (g m^{-2} s^{-1}) and LE is the latent heat flux (W m^{-2}).

We selected the best performing TSEB/DTD variant and radiometric surface temperature output (compared against EC estimates) to produce spatially distributed ET values. Each LE pixel was converted to ET using the bigleaf package for R (Knauer et al., 2018), using the relevant air temperature values from EC stations. The ET rasters were then averaged by the corresponding EC station footprint. The linear relationship between UAS and EC-derived ET was ascertained using regression analysis, and the slope and intercept coefficients were used to calibrate the final UAS ET estimates.

2.4.7. Explanatory variables and sampling approach

With the new spatial and temporal detail to energy and water flux mapping provided by the UAS compared to EC station and satellite remote sensing approaches, we examined some of the environmental and biophysical drivers of evapotranspiration variability at our study site. We devised our sampling approach to examine how ET varied as a function of 1) time of day, 2) date, 3) vegetation type (tree or grass canopy), 4) elevation, 5) fertilizer treatment, and for trees 6) crown area and 7) tree height.

We sampled vegetation at a network of points across the tree and grass strata throughout the site. In total, 2517 tree canopies were identified in the UAS imagery using the CHM to delineate crown areas and treetop sampling points using the lidR and treetop packages in R (Roussel and Auty, 2021). An equal number of sampling points were randomly distributed across the site using the grass processing mask to limit their distribution, as displayed in Fig. 1. Areas around the tracks were discounted for grass sampling points, as the bare soil would influence ET readings.

Here the temporal dimension (day, date) encompasses all of the random variability brought about by changing meteorological forcings and biophysical properties of the vegetation that may be associated with the temporal evolution of the vegetation (Figs. 2 and 3 highlight this variability). Given that many of these properties are used as, or correlated with, TSEB model inputs, we simply use time/date as general proxies for changing conditions, and test these as random variables.

Spatial variables were extracted for each sampling point from the following datasets: vegetation type was derived from the tree/grass masks, elevation was taken from the DTM for grass, and CHM minus tree height for trees, fertilizer treatment was conservatively delineated using average footprints around each tall EC station tower (N, C, and NP), all other points were classed as "O" (other), and tree height and crown diameter were derived from the CHM using the treetop package. All sampling points were then used to extract ET values using the raster package for R (Hijmans et al., 2021) and each ET value was assigned a relevant time and date stamp according to when the data were collected. The dataframe was then merged using the reshape2 package for R (Wickham, 2007) so that each response value (ET) had the corresponding explanatory variables on the same row.

To test the effects of the drivers (1–7) outlined above, the dataset had to be subsetted to ensure fair comparability between variables. For example, to examine the effect of survey date, and thus senescence, it was necessary to standardize the time of day, so only data from midday surveys were selected for this analysis. Table 3 outlines the datasets and models used in each analysis. Correlation between explanatory variables was assessed using the GGally package (Schloerke et al., 2021) in R; the only covariates were tree height and crown area. Given that crown area is observable from both aerial and satellite imagery, whereas tree height can be quickly estimated from the ground compared to crown area (e.g. using a clinometer), we explore both variables in Model 4.

2.4.8. Statistical analyses

We used Generalised Linear Mixed effect Models (GLMMs) of the Gaussian family (owing to the normal distribution of ET data) to test which explanatory variables (outlined in Section 2.4.7) were significant drivers of UAS-derived evapotranspiration on the tree grass ecosystem site at Majadas. GLMMs are suitable for evaluating both continuous (time or space) and categorical variables, which can be tested for their individual explanatory power, as well as their interactions with other variables. Here we differentiate between fixed and random explanatory variables, with fixed variables being accurately measured treatments, categories or variables, and random effects being temporal proxies (time of day, date of survey) which embody a wide range of potential variability. Explanatory variables were tested in R using backward selection, until only significant predictors remained in the model. Akaike's Information Criterion (AIC) values were used to select the most parsimonious model. We also used a non-parametric Generalised Additive Model to assess the non-linear effects of time on ET, using a smoothing function set to 3 degrees of freedom, to avoid model overfitting.

3. Results

3.1. Land surface temperature estimation

We first tested the accuracy of the different methods for deriving radiometric surface temperature from the UAS thermal imagery. Compared to the spatially and temporally coincident reference surface temperatures measured using the Apogee Infrared radiometer, the radiometric surface temperature method with the lowest error was the empirical method T_{EMP} (RMSD 2.62 K, bias −0.44 K, standard deviation 2.66 K), followed by T_{RAW} (RMSD 4.21 K, bias 2.40 K, standard deviation 3.56 K), and T_{LST} (RMSD 13.51 K, bias 9.11 K, standard deviation 10.46 K).

3.2. EC station-UAS flux comparison

Latent heat flux describes the energy consumed during ET, and is thus the most important flux for mapping ET Eqs. (4) and ((5)). *LE* was most accurately captured using the Dual Time Difference (DTD) model in conjunction with the empirical method for deriving radiometric surface temperature T_{EMP}, as demonstrated by its low RMSD, bias, standard deviation (Tables 4 and S1), and high R^2, slope close to 1, and low intercept (Fig. 4a). The EC-UAS agreement in *LE* was especially strong for the sub-canopy layer (grass only), with an RMSD of 51 W m^{-2}, slope 0.93, and R^2 0.81 (Fig. 5).

Although the DTD-T_{EMP} combination did not yield the best estimates of *Rn, H*, and *G*, we use this model because our study focuses on ET mapping. Fig. 5 shows overestimation/underestimation of *LE/H* compared to the above canopy towers, with the converse being true for sub-canopy towers.

3.3. Factors affecting evapotranspiration

3.3.1. Temporal trends

Here we divide temporal trends in ET into two time scales; ET as a function of time of day and date of survey (Model 1), and control for time of day to assess survey date in Model 2. Model 1′s explanatory power was substantial (adjusted R^2 0.68, 95% CI 0.06, $P < 0.001$), with ET in trees being significantly higher than grass across the survey period ($\beta = 0.02$, $\tau = 117.3$, $P < 0.001$). Time of the day was a statistically significant smooth term in the model, with ET peaking around midday in both grass and trees, then falling towards the evening (effective degrees of freedom = 2 and 2, $F = 7379$ and 17,607, $P < 0.001$ and $P < 0.001$ respectively), although ET in trees is much greater (Fig. 6a). The advantage of using a UAS to map ET is that we can also map these temporal changes. Fig. 7 shows how ET evolves throughout the day, from very low values at around 10:00 (Fig. 7a), building towards the

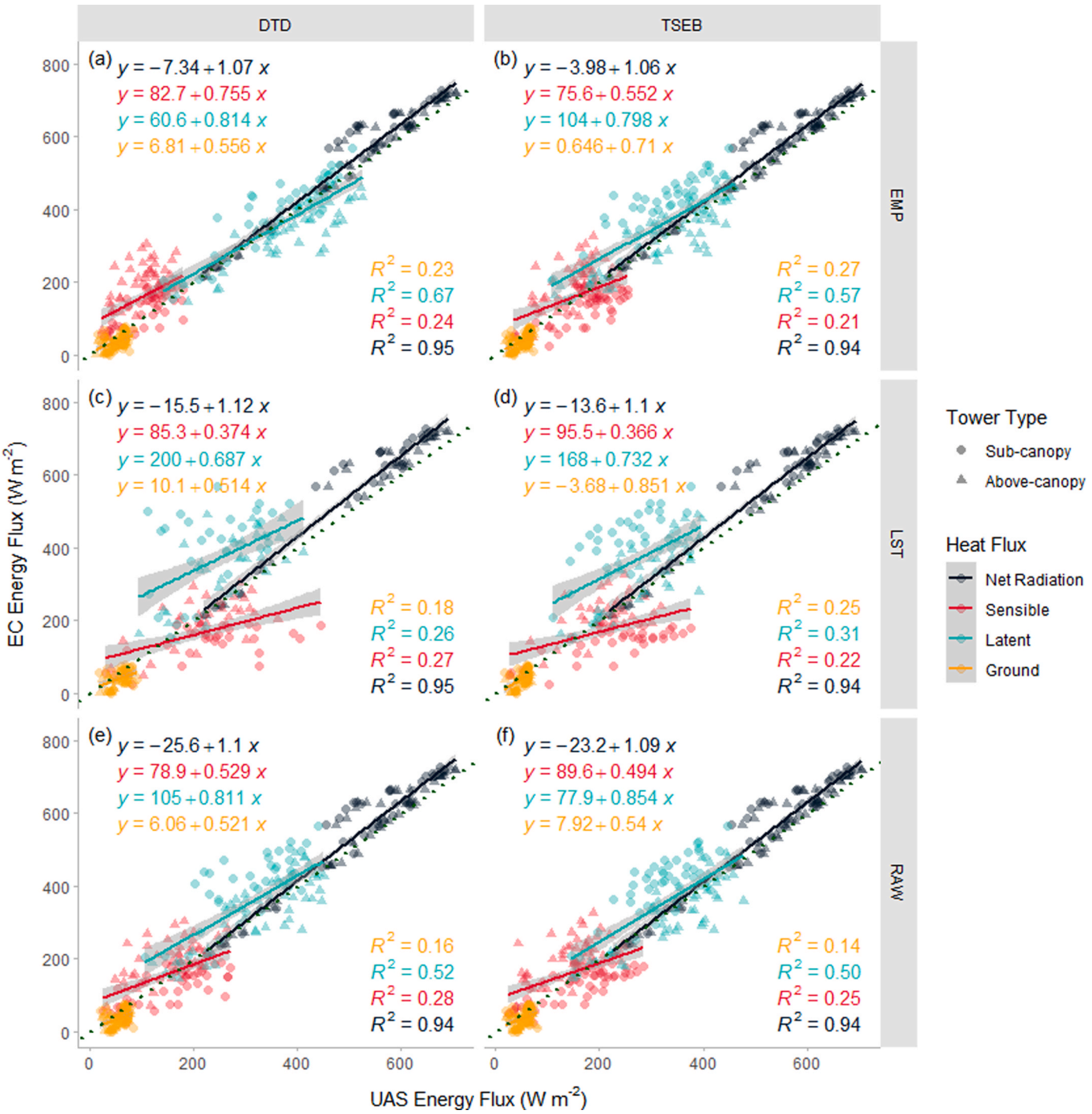

Fig. 4. Flux mapping performance of the UAS (predicted) compared to the Eddy Covariance (EC) measurements (observed). The plots highlight how different methods of deriving radiometric surface temperature, T_{EMP} (Empirical relationship) (a, b), T_{LST} (emissivity and transmittance corrected land surface temperature) (c, d), and T_{RAW} (radiometric surface temperature) (e, f) influence UAS flux accuracy. Also shown are how the two modeling methods, DTD (Dual Time Difference) (a, c, e) and TSEB (Two-Source Energy Balance) (b, d, f) influence UAS derived flux accuracy. Plots show data from the sub-tree canopy (●) and above-tree canopy (▲) EC stations, where the sub-tree canopy comparison are grass only, and above-tree canopy comparisons include tree and grass. Plotted using custom routines from (Aphalo, 2021, https://github.com/aphalo/ggpmisc).

peak at 14:30, then ET is reduced again by 16:30. By 16:30 the grassy areas return to similar ET values as 11:30, however ET in trees remains higher after the daily peak.

By observing ET values from around midday only (11:30 – 13:00), it is then possible to examine how ET responded over the survey period in Model 2. As this subsetted dataset is also suitable for comparing the effects of elevation, and vegetation type, these variables are included in the model. As there is some variability in survey times for each date, we treat time of day as a random variable. The model's explanatory power including fixed and random variables was substantial (conditional $R^2 = 0.63$), as was the part related to the fixed variable alone (marginal $R^2 = 0.30$). There was a significant interaction between date and vegetation, with ET in trees increasing significantly more over the survey period than grass (coefficient = 0.02, 95% CI = 0.002, $t = 42.85$, d.f. = 16,157, $P < 0.001$), see Fig. 6b. These patterns are clearly visible in the ET maps in Fig. 8, where tree and grass ET values are similar in the first two

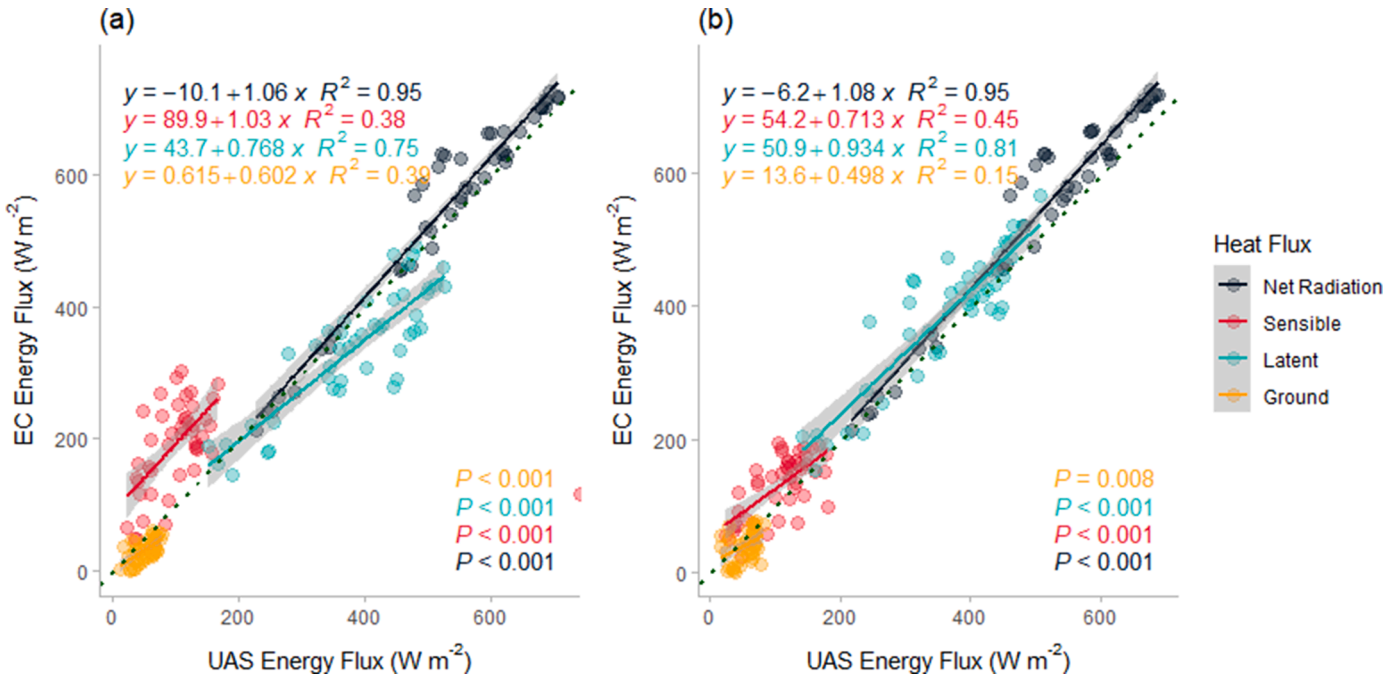

Fig. 5. (a) Above-tree and (b) sub-tree canopy flux comparisons between UAS and Eddy Covariance (EC) using the Dual Time Difference (DTD) energy balance model with empirical thermal calibration method (T_{EMP}), with linear trend lines (colored) and standard error (gray shading). (For interpretation of the references to color in this figure legend, the reader is referred to the web version of this article.)

timesteps (05/05/2021 and 11/05/2021), however ET in the trees continually increases as the survey period progresses. Evidence of grass senescence is also visible in Fig. 8e, with extensive areas showing lower ET values. The variability of ET values increases in grass towards the end of the survey period Fig. 6b, which reflects the patchiness of the grass canopy (Fig. 8e). While there was also a significant interaction between date and elevation, this and other spatial trends will be presented in the following section.

3.3.2. *Spatial trends*

The effects of elevation were mediated by survey date; i.e. in Model 2 there was a statistically significant but weak negative interaction effect of date and elevation on ET for the grass canopy (std. coeff. = −0.007, std. 95% CI = −0.01- −0.01, t = −6.94, d.f. = 16,154, $P < 0.001$). As the survey period progressed, ET in the lower elevations increased more than higher elevations, especially in trees (Fig. 9a). The spatial distribution of these differences are plotted in Fig. 10, showing an overall positive change in ET in trees, and in much of the grassland areas. While there were isolated areas of grass at lower elevations showing a negative trend in ET (i.e. between N and C EC stations), the majority are at high elevations. Compared to grass, the effect of elevation over the survey period was less important for trees (std. coef = −0.03, std. 95% CI = −0.05- −0.01, t = −3.26, d.f. = 16,254, P < 0.05).

The GLMM model used for assessing the effect of fertilizer treatments (Model 3) yielded reasonable and significant explanatory power (conditional R^2 = 0.62, marginal R^2 = 0.26). As shown in Fig. 9(b), the effects of both fertilizer treatments (addition of N and NP) on ET were significantly higher than the control (C) for both trees and grass (for N std. coeff = 0.4, std. 95% CI = 0.33–0.46, t = 11.69, d.f. = 5047, $P <$ 0.001 and for NP std. coeff. = 0.41, std. 95% CI = 0.34–0.47, t = 11.68, d.f. =5047, $P <$ 0.001), however the fertilizer effect was weaker for trees (for N std coeff. = −0.21, std. 95% CI = −0.30- −0.11, t = −4.41, d.f. = 5047, $P <$ 0.001) and the NP treatment was not significantly different to N (std. coeff. = −0.03, std. 95% CI = −0.11- −0.06, t = −0.64, d.f. = 5047, P = 0.512). These effects are seen in Fig. 11, which shows the midday ET for the three fertilizer treatments at the beginning and end of the survey period. The most evident effect is between the control and the two fertilizer treatments (Fig. 11c,d) vs (Fig. 11a,b) and (Fig. 11c,d) vs (Fig. 11e,f), where differences in ET between treatments is especially greater in grass compared to trees especially at end of the survey period.

Model 4 was used to investigate how tree structural properties can influence ET, the model's explanatory power of fixed effects (tree height and crown area) was very weak, but significant (marginal R^2 = 0.01, $P <$ 0.001). There was no significant interaction between tree height and canopy area on ET response, despite their correlation. The random effects of date and time were large, with a conditional R^2 = 0.64. The spatial effects of crown area and height were very weak, but also positive and significant (std. coeff = 0.08, std. 95% CI = 0.06–0.1, t = 8.12, d.f. = 6195, $P <$ 0.001, and std. coeff = 0.05, std. 95% CI = 0.04, 0.07, t = 5.67, d.f. = 6195, $P <$ 0.001 respectively). These very weak trends can be observed in Fig. 9c and 9d.

4. Discussion

We provide the largest number of EC-UAS derived energy flux comparisons to date (324), showing significant spatial and temporal patterns of ET across a temperate oak savanna site during the senescence period in 2021. We clearly show how ET in trees and grass responds differentially during the day, during the progression of the senescence period, and in response to different fertilizer treatments. We use temporality as a proxy for the changing meteorological and environmental conditions experienced both within and across days (Figs. 2 and 3). Unsurprisingly, ET peaks in both grass and trees around solar noon (Figs. 7a and 8e), with ET in trees being significantly higher than grass at all times. Over the survey period there was a significant and marked increase in ET for trees, however the signal was far weaker for grass (Fig. 6b). This can be explained by the interaction between a trend towards environmental conditions that promote higher ET, e.g., increased air temperature, vapor pressure deficit (VPD), and incoming radiation (Fig. 2), and higher water availability in trees due to their deeper roots compared to grass (El-Madany et al., 2020). In two previous studies at the same site at Majadas de Tietar, Burchard-Levine et al. (2021) yielded accurate flux estimates of the TGE (compared to EC stations) using

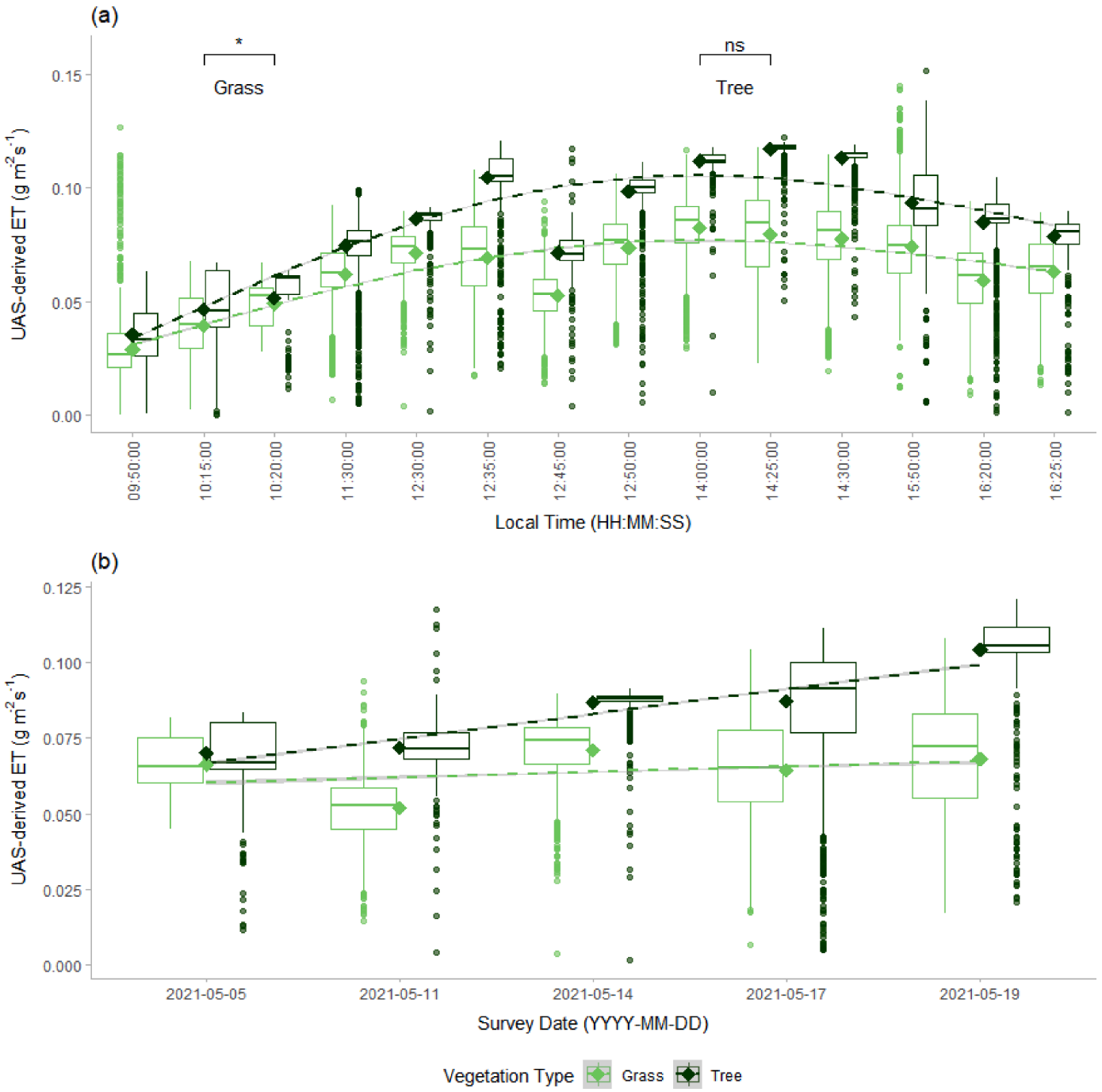

Fig. 6. Temporal trends of Evapotranspiration (ET) as a function of vegetation type, and (a) time of day, and (b) survey date. The boxplots show the ET distribution for the sampling points marked in Fig. 1. All pairs are different with high significance ($P<0.001$) except those marked. Diamond points (◆) denote the mean, and dashed lines denote trendlines from the generalised models described in Section 2.4.7.

airborne LST data at 4.5 m, and resampled to 1.5 m ground sampling distance, which enabled them to separate tree and grass canopies. While their flux estimate accuracies were comparable to ours (RMSD ≈ 60 W m^{-2} for LE), their overpass return interval was far greater (months apart), perhaps owing to the cost and logistical limitations of using manned aircraft. In another study, El-Madany et al. (2018) demonstrated the sensitivity of the EC method to associate temporal flux variability to surface characteristics, however the method does not allow spatial separation of grass and tree canopies. Given that our approach still relies on EC station data for model inputs, as well as calibration and validation purposes, the UAS method should be seen as complimentary. Although model input data could be collected using mobile weather stations, radiometers, and pyranometers, further work is required in order to calibrate accurate UAS energy and water estimates completely independent of EC stations.

We report fertilizer treatment as a significant driver of ET in the TGE, in agreement with previous work (El-Madany et al., 2021; Luo et al., 2020). The effects are most prominent in the grass canopy where the addition of nitrogen and nitrogen phosphorus yielded significantly higher ET values compared to the control area (Figs. 9b, and 11). The addition of NP significantly increased ET in grass compared to N alone, however this effect was non-significant in trees. These overall results can be explained using previous studies (El-Madany et al., 2021; Luo et al., 2020; Migliavacca et al., 2017) that showed significantly higher

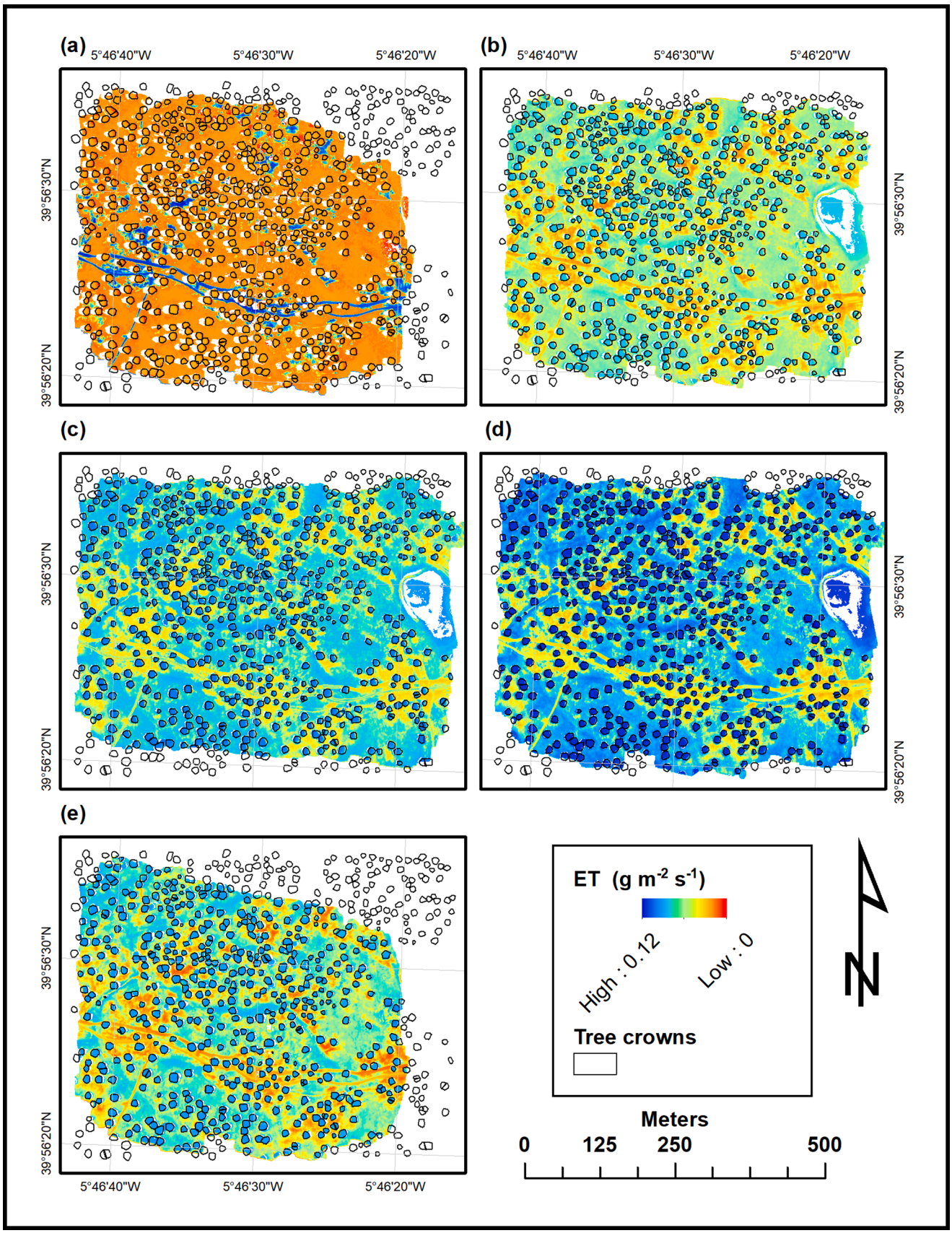

Fig. 7. Evapotranspiration (ET) maps from 17/05/2021 of the Tree-Grass Ecosystem (TGE) at the Control fertilizer treatment site tower. Temporal changes in ET through a single day, at (a) 0950, (b) 1130, (c) 1250, (d) 1430, and (d) 1620 are shown. The higher ET values seen on the tracks in plot (a) are artifacts caused early in the morning when the tracks were warmed. Gray polygons denote tree crowns, Projected Coordinate System = WGS84 UTM 30 N.

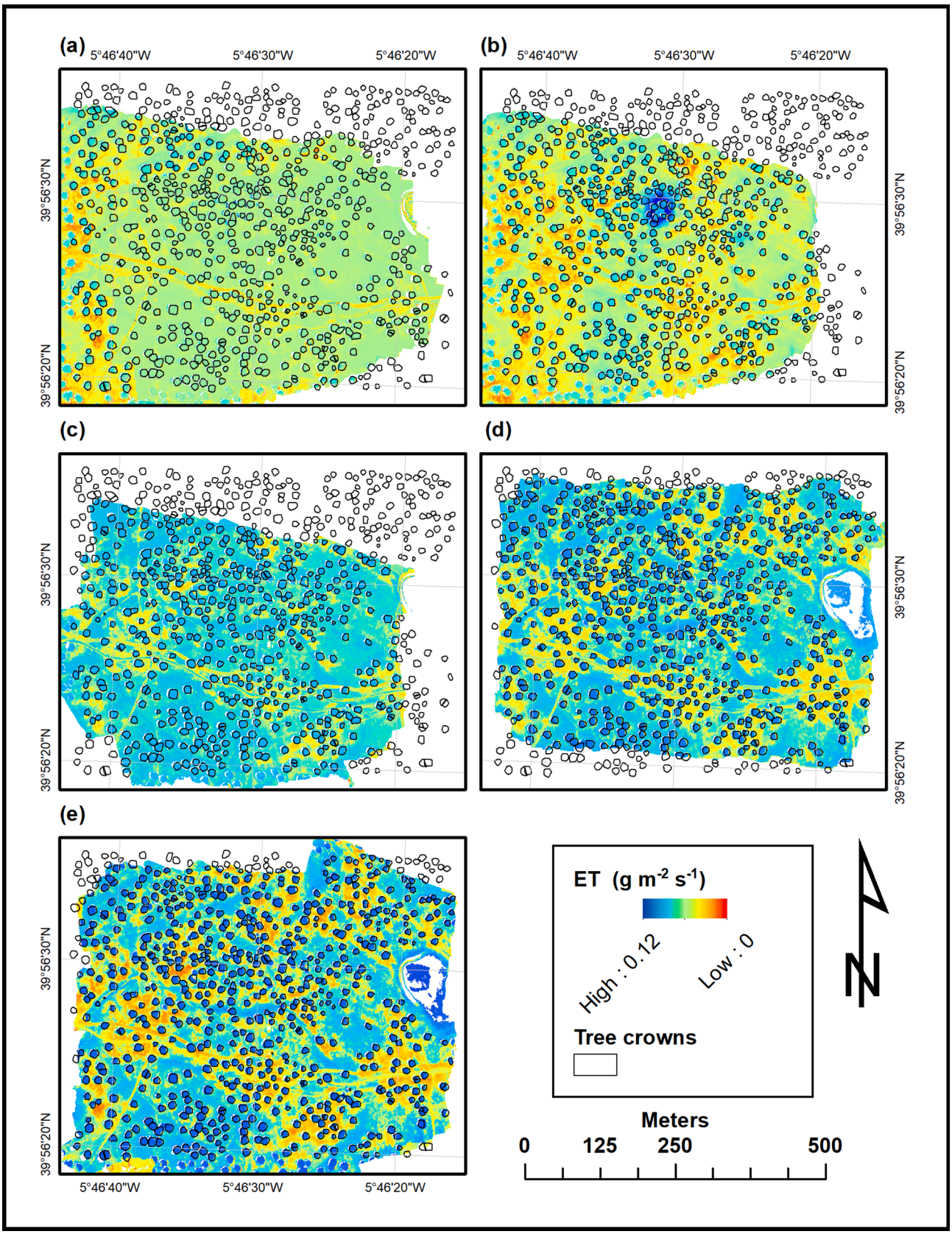

Fig. 8. Development of Evapotranspiration (ET) during the survey periods in the Tree-Grass Ecosystem (TGE), on (a) 05/05/2021, (b) 11/05/2021, (c) 14/05/2021, (d) 17/05/2021 and (e) 19/05/2021. The maps show ET measured at midday (± 1 hour) only.

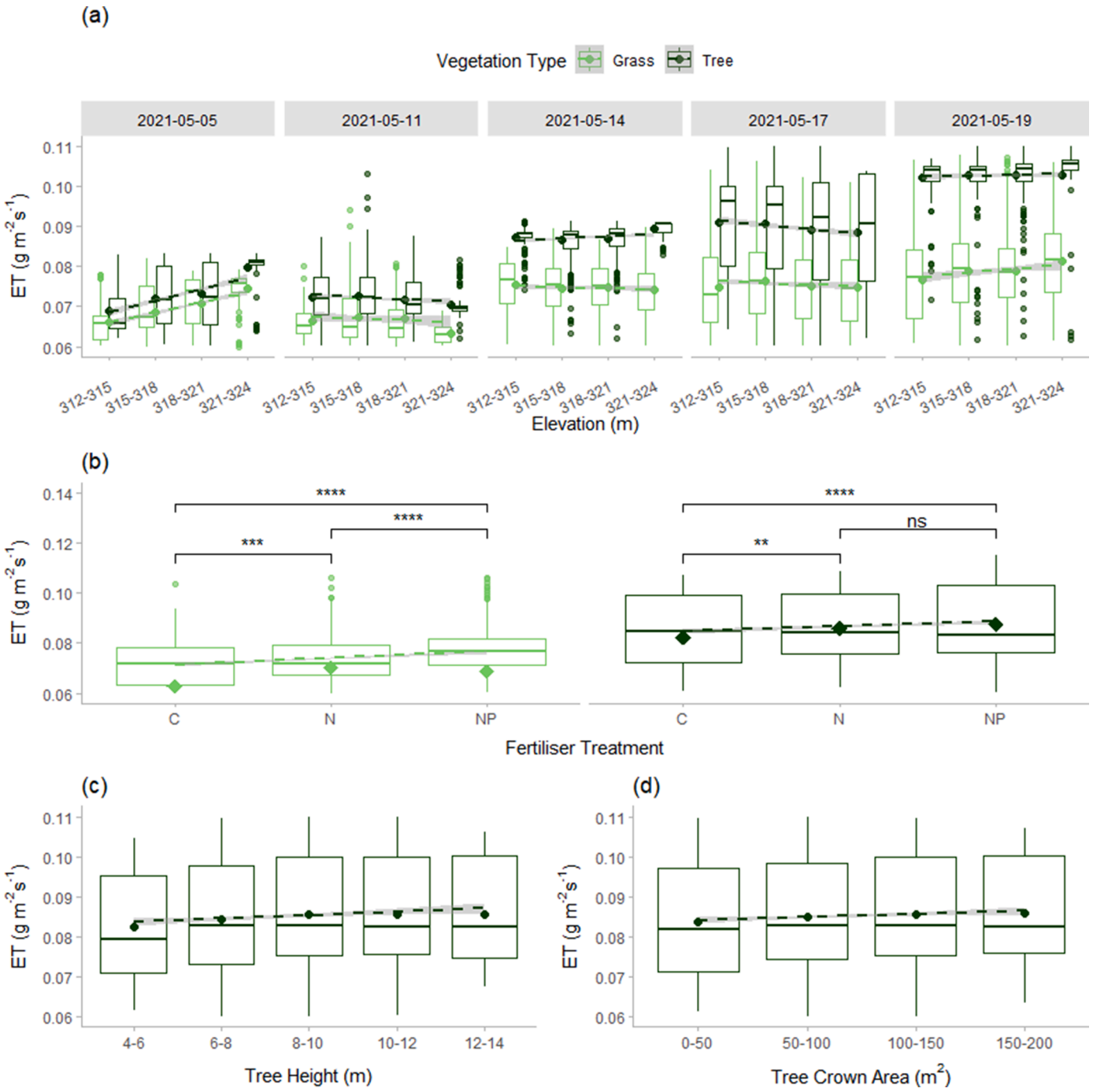

Fig. 9. Spatial drivers of Evapotranspiration (ET) variability in a tree-grass ecosystem. The effect of elevation (proxy for position on the hill) was very weak but significant in Model 2. (height above ellipsoid shown). Subplot (a) shows a tendency for lower ET at lower elevations early in the survey period, however this trend weakens after 11/05/2021 where ET at lower elevations is similar or greater than that of higher elevations. The large increase in ET between 11/05/2021 and 14/05/2021 corresponds to an increase in air temperature and incoming radiation (Fig. 2.). In (b) we show ET values in grass and trees over three different fertilizer treatment sites (C = Control, *N* = Nitrogen-added, NP = Nitrogen-Phosphorous-added) as well as the significance of difference between means. Subplot (c) shows ET as a function of tree height (Model 3), while (d) presents ET as a function of tree crown area (Model 4). Sample sizes can be found in Table 3.

chlorophyll $a + b$ (Cab), canopy nitrogen content (N%), and maximum carboxylation capacity (V_{cmax}) in N and NP fertilized grass canopies compared to the control over the same time period in 2014. Higher levels of these metabolic plant functional traits are linked to increases in gross primary productivity, photosynthesis and consequently transpiration rates. Also, an increase of LAI as consequence of N fertilization led to increased grass transpiration (El-Madany et al., 2021; Luo et al., 2020), that at the experimental site led to an earlier senescence in the N treatment because of faster depletion of soil moisture (Luo et al., 2020).

While previous studies have detected ET differences in fruit trees as a response to different watering treatments (Park et al., 2017), or under different nutrient treatments (El-Madany et al., 2021) we are the first to assess the effects of fertilizer treatment on ET using the UAS approach. Our results show an important application for the UAS ET mapping method in understanding how land management practices can affect water use and the surface energy balance. These methods would be particularly useful for understanding how agroforestry practices (Kuyah et al., 2019), land use change (Heald and Spracklen, 2015), and different

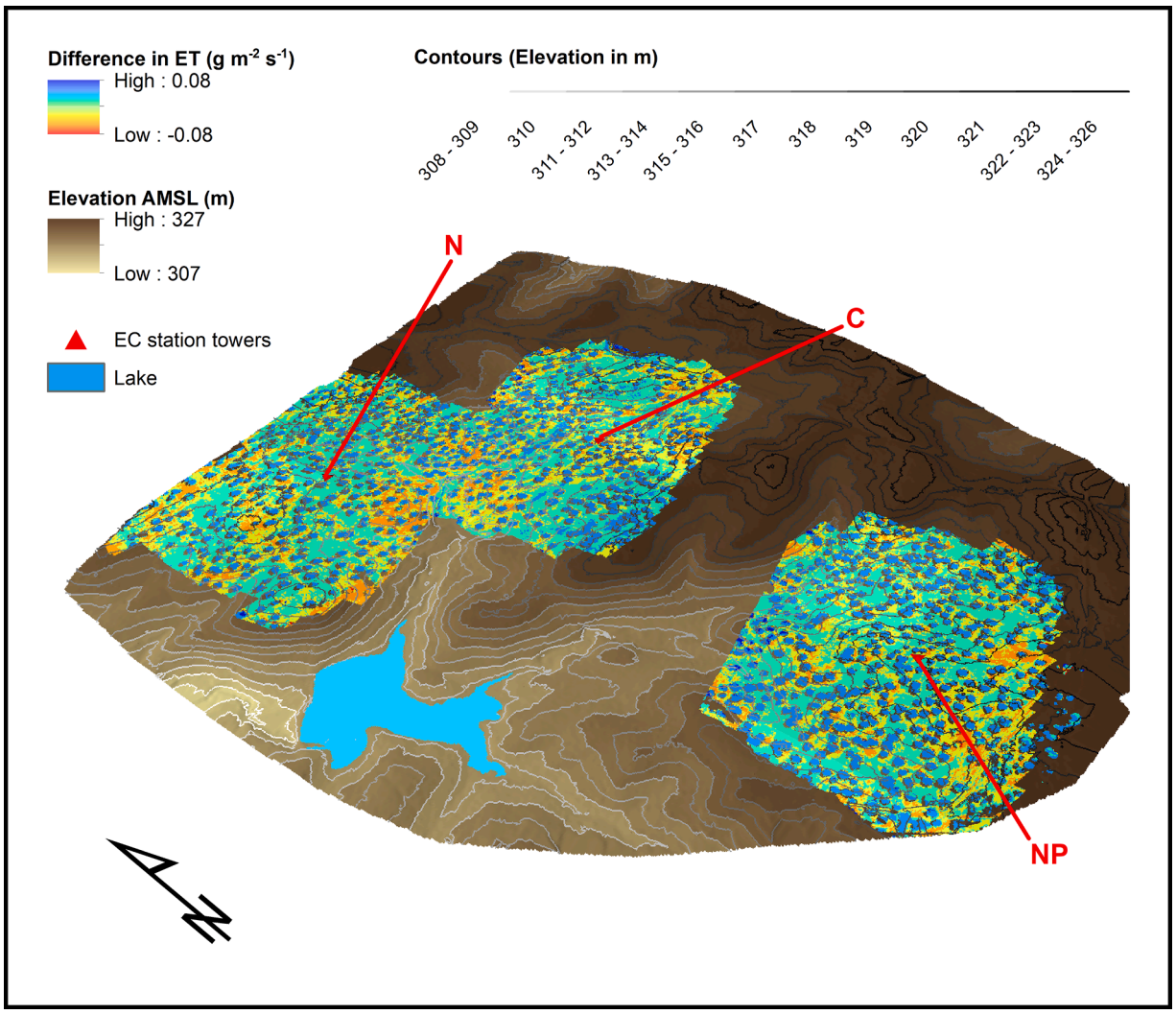

Fig. 10. Spatial distributions of midday estimated Evapotranspiration change over the entire period of this study (05/05/2021 – 19/05/2021). The three fertilizer treatment sites are denoted as C = Control, *N* = Nitrogen-added, NP = Nitrogen-Phosphorous-added, and data is overlaid on a topographic map of the site.

irrigation practices (Sugita et al., 2017) can influence energy fluxes and ET. This method would also be practical for researching drought resistant crops, or monitoring the establishment of afforestation/reforestation projects (Wheeler et al., 2021) where sapling mortality has been reportedly high (e.g., Coleman et al., 2021). While others have successfully mapped biomass and yield traits using remote sensing methods (Yang et al., 2020), we demonstrate a method for mapping ET which would enable researchers and land users to map water use efficiency, e.g., as biomass or yield gain per unit evapotranspiration, at new temporal and spatial resolutions. High fidelity and resolution UAS ET datasets could also be used to evaluate and calibrate lower resolution spaceborne remote sensing data and earth system model output that typically have a resolution $\leq$1 km. Within one pixel there could be multiple farms, land uses and vegetation types, each contributing differentially to the surface energy and water balance. Without understanding this sub-grid heterogeneity, it is not possible to disentangle the drivers of flux heterogeneity.

We also assessed how elevation, tree height and crown area influenced ET, these however were less important than vegetation type, short- and long-term environmental variations and fertilizer treatment. These results are unsurprising because the site is relatively flat (elevation 317.6 $\pm$ 2.3 m), and the trees are relatively homogeneous in stature (tree height 8.56 $\pm$ 1.3 m, crown area 93.6 m^2 $\pm$ 32 m^2). Nevertheless, small but significant signals were detected. The elevation and date interaction may be driven by the changes in water availability as the survey period progressed, that is, areas lower down the hill possibly remained wetter for longer than the tops of the hills. This would explain the equalization in ET between tops and bottoms of the hill on the last days of the surveys. A possible explanation for the increased response of ET with tree height and crown dimensions may be firstly that larger trees may have deeper roots, and are thus less water limited, together with the fact that these taller canopies are also better coupled with the atmosphere, and with larger LAI values, and therefore they are more effective in dissipating heat. This phenomenon may also be an artifact of LST retrieval methods, whereby smaller trees have a higher circumference to surface area ratio. Therefore, warmer (grass) pixels surrounding the trees may have more influence on the interior pixels of the tree, i.e., an edge effect (FLIR, 2018). While we addressed this effect by removing pixels from around tree edges, the effect may be unavoidable for the smallest trees.

While we followed the protocols of Heinemann et al. (2020) for LST retrieval using UAS thermal infrared cameras, the T_{LST} datasets had the largest errors compared to our ground control measurements. It is possible that this method is unsuitable for LST derivation on vegetation types other than dense crop, especially as the method does not account for the emissivity of senescent vegetation. We achieve reasonable LE accuracies using the correction coefficients derived in (Simpson et al., 2021), but also using the factory correction factor (T_{RAW}). A noteworthy

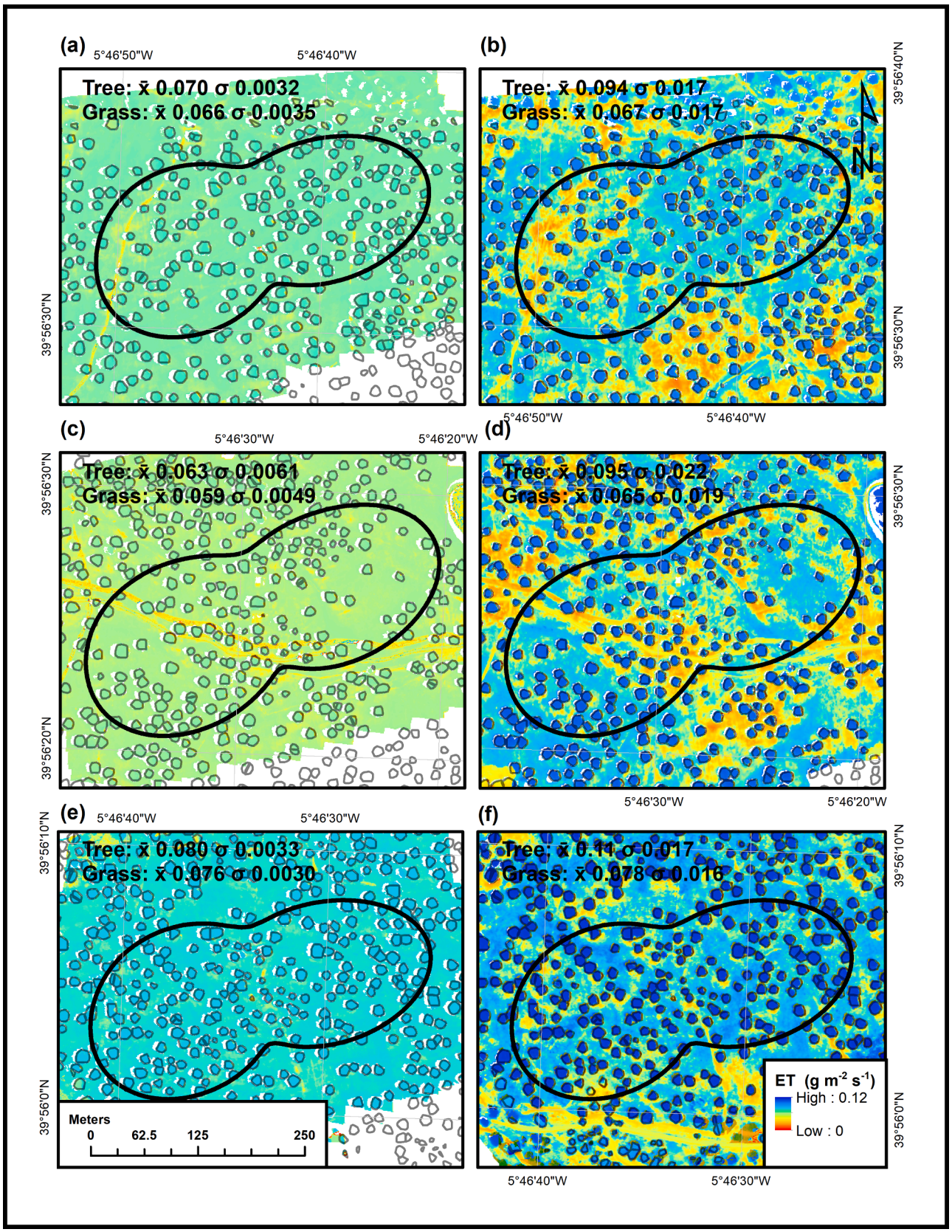

Fig. 11. The effects of three fertilizer treatments on Evapotranspiration (ET), namely Nitrogen-added (a, b), Control (c, d), and Nitrogen-Phosphorous-added (e, f). The maps show midday ET from two survey dates at the beginning, 05/05/2021 (a, c, e), and the end 10/05/2021 (b, d, f) of the study. Mean ($\bar{x}$) and standard deviation (1σ) ET statistics are reported in each panel for both canopy layers. Layers are displayed in PCS WGS 84 UTM 30 N.

pattern emerged in our accuracy assessment; the above canopy EC stations encompassing both tree and grass fluxes yielded slightly poorer LE agreement than the below-canopy EC stations. This is perhaps owing to the cooling effects of tree shadows affecting EC station measurements, but not UAS estimates where the shadows are masked. While the DTD method was used to derive ET layers for analysis, similar accuracies are reported using the TSEB-PT method, where there is no need to collect a radiometric surface temperature dataset shortly after sunrise, however if this approach is used we recommend that some calibration of the thermal infrared camera is conducted, either using a black body reference (Kelly et al., 2019), or an empirical method as in Simpson et al. (2021). Given the errors in the DTD and TSEB-PT methods were similar, even when less accurate LST data were used (Fig. 4), this suggests that model uncertainty may be driven by other input sources such as LAI and green fraction, especially during the end of the survey when senescence develops. Further work on improving these datasets could yield further accuracy benefits.

5. Conclusions

In this study, we demonstrated the utility of an integrated multispectral-thermal infrared unmanned aerial system for deriving very high-resolution gridded evapotranspiration estimates using the TSEB and DTD models. Given the high sensitivity, spatial (< 1 m), and temporal resolution of these estimates, we were able to investigate some of the drivers of ET change in a tree-grass savanna ecosystem during a seasonal transition phase (spring-summer). As increased environmental pressures such climate extremes (Hatfield et al., 2014) and landscape fragmentation can exacerbate water shortages (Ewers and Banks-Leite, 2013; Osborne et al., 2018), there is a need to better understand how different configurations of canopy height, plant functional groups, e.g., in an agroforestry context, and land management practices, e.g. applications of fertilizer or irrigation, influence water use in real-world scenarios. Here the UAS becomes an invaluable tool alongside eddy covariance measurements and satellite estimates, respectively addressing the spatial and temporal limitations of each approach. By measuring land-atmosphere interactions at multiple scales we may reduce uncertainty in, e.g., future climate change projections. This field of research has the potential to leverage a number of Sustainable Development Goals, e.g. SDG 2 (Zero Hunger), SDG 6 (Clean Water and Sanitation), SDG 13 (Climate Action) and SDG 15 (Life on Land) (UNEP, 2019).

Financial support

This research was supported by the DAAD/BMBF program Make Our Planet Great Again – German Research Initiative Project MONSOON (grant number 57429870).

Data availability statement

The UAS-derived TSEB/DTD input and output datasets are freely available for download at https://doi.org/10.5281/zenodo.5554073.

CRediT authorship contribution statement

Jake E. Simpson: Conceptualization, Data curation, Formal analysis, Methodology, Project administration, Software, Visualization, Writing – original draft, Writing – review & editing. **Fenner H. Holman:** Conceptualization, Data curation, Formal analysis, Methodology, Formal analysis, Project administration, Writing – review & editing, Software, Writing – review & editing. **Hector Nieto:** Methodology, Software, Writing – review & editing. **Tarek S. El-Madany:** Data curation, Methodology, Software, Writing – review & editing. **Mirco Migliavacca:** Data curation, Methodology, Writing – review & editing. **M. Pilar Martin:** Data curation, Methodology, Project administration, Writing – review & editing, Resources. **Vicente Burchard-Levine:** Data curation, Writing – review & editing. **Arnaud Cararra:** Project administration, Writing – review & editing, Resources. **Solveig Blöcher:** Software, Writing – review & editing. **Peter Fiener:** Project administration, Writing – review & editing. **Jed O. Kaplan:** Conceptualization, Funding acquisition, Project administration, Writing – review & editing, Resources.

Declaration of Competing Interest

None.

Acknowledgments

The authors would like to acknowledge the MONSOON Project team, Benjamin Bukombe for his assistance with the statistical analysis, and Krzysztof Bluszcz for his patience and support.

Supplementary materials

Supplementary material associated with this article can be found, in the online version, at doi:10.1016/j.agrformet.2022.108981.

References

Alhassan, A., Jin, M., 2020. Evapotranspiration in the Tono Reservoir Catchment in Upper East Region of Ghana estimated by a Novel TSEB approach from ASTER imagery. Remote Sens. (Basel) 12 (3), 569. -569.
Allen, R.G., Pereira, L.S., Raes, D., Smith, M., 1998. Chapter 4 - Determination of ETo. Rome.
Aphalo, P.J., 2021. ggpmisc: miscellaneous Extensions to 'ggplot2'.
Arnault, J., Knoche, R., Wei, J., Kunstmann, H., 2016. Evaporation tagging and atmospheric water budget analysis with WRF: a regional precipitation recycling study for West Africa. Water Resour. Res. 52 (3), 1544–1567.
Barcza, Z., Kern, A., Haszpra, L., Kljun, N., 2009. Spatial representativeness of tall tower eddy covariance measurements using remote sensing and footprint analysis. Agric. For. Meteorol. 149 (5), 795–807.
Bellvert, J., et al., 2021. Remote sensing energy balance model for the assessment of crop evapotranspiration and water status in an almond rootstock collection. Front. Plant. Sci. 12, 288. -288.
Bogdanovich, E., et al., 2021. Using terrestrial laser scanning for characterizing tree structural parameters and their changes under different management in a Mediterranean open woodland. For. Ecol. Manage. 486, 118945. -118945.
Brenner, C., Zeeman, M., Bernhardt, M., Schulz, K., 2018. Estimation of evapotranspiration of temperate grassland based on high-resolution thermal and visible range imagery from unmanned aerial systems. Int. J. Remote Sens. 39 (15–16), 5141–5174.
Burchard-Levine, V., et al., 2022. A remote sensing-based three-source energy balance model to improve global estimations of evapotranspiration in semi-arid tree-grass ecosystems. Glob. Chang. Biol. 28 (4), 1493–1515.
Burchard-Levine, V., et al., 2021. The effect of pixel heterogeneity for remote sensing based retrievals of evapotranspiration in a semi-arid tree-grass ecosystem. Remote Sens. Environ. 260 (April).
Burchard-Levine, V., et al., 2019. Adapting the thermal-based two-source energy balance model to estimate energy fluxes in a complex tree-grass ecosystem. Hydrol. Earth Syst. Sci. Discussions(August) 1–37.
Burchard-Levine, V., et al., 2020. Seasonal adaptation of the thermal-based two-source energy balance model for estimating evapotranspiration in a semiarid tree-grass ecosystem. Remote Sens. (Basel) 12 (6).
Chao, L., Zhang, K., Wang, J., Feng, J., Zhang, M., 2021. A Comprehensive evaluation of five evapotranspiration datasets based on ground and GRACE satellite observations: implications for improvement of evapotranspiration retrieval algorithm. Remote Sen. 2021 13 (12), 2414. Vol. 13, Page 2414-2414.
Coleman, E.A., et al., 2021. Limited effects of tree planting on forest canopy cover and rural livelihoods in Northern India. Nat. Sustain. 2021, 1–8.
Ekern, P.C., Robins, J.S., Staple, W.J., 2015. Soil and cultural factors affecting evapotranspiration. Irrigat. Agric. Lands 11, 522–533.
El-Madany, T.S. et al., 2020. Drought and heatwave impacts on semi-arid ecosystems' carbon fluxes along a precipitation gradient: drought and Heatwave Impacts.
El-Madany, T.S., et al., 2021. How nitrogen and phosphorus availability change water use efficiency in a Mediterranean Savanna Ecosystem. J. Geophys. Res. 126 (5) e2020JG006005-e2020JG006005.
El-Madany, T.S., et al., 2018. Drivers of spatio-temporal variability of carbon dioxide and energy fluxes in a Mediterranean savanna ecosystem. Agric. For. Meteorol. 262, 258–278.
Ellison, D., et al., 2017. Trees, forests and water: cool insights for a hot world. Glob. Environ. Change 43, 51–61.
Ewers, R.M., Banks-Leite, C., 2013. Fragmentation impairs the microclimate buffering effect of tropical forests. PLoS ONE 8 (3), e58093. -e58093.

Famiglietti, J.S., Wood, E.F., 1991. Evapotranspiration and runoff from large land areas: land surface hydrology for atmospheric general circulation models. Surv. Geophys. (12), 179–204.
Feng, S., et al., 2020. A global quantitation of factors affecting evapotranspiration variability. J. Hydrol. (Amst) 584, 124688. -124688.
Fersch, B., et al., 2020. High-resolution fully coupled atmospheric-hydrological modeling: a cross-compartment regional water and energy cycle evaluation. Hydrol. Earth Syst. Sci. 24 (5), 2457–2481.
Fisher, J.B., et al., 2017. The future of evapotranspiration: global requirements for ecosystem functioning, carbon and climate feedbacks, agricultural management, and water resources. Water Resour. Res. 53 (4), 2618–2626.
FLIR, 2018. Radiometric Temperature Measurements: surface characteristics and atmospheric compensation.
Foken, T., Aubinet, M., Leuning, R., 2012. The eddy covariance method (Editors). In: Aubinet, M., Vesala, T., Papale, D. (Eds.), Eddy Covariance: A Practical Guide to Measurement and Data Analysis. Springer Netherlands, Dordrecht, pp. 1–19.
Gates, D.M., Hanks, R.J., 2015. Plant factors affecting evapotranspiration. Irrigat. Agric. Lands 11, 506–521.
Gebler, S., et al., 2015. Actual evapotranspiration and precipitation measured by lysimeters: a comparison with eddy covariance and tipping bucket. Hydrol. Earth Syst. Sci. 19, 2145–2161.
Girardeau-Montaut, D., 2021. CloudCompare: 3D point cloud and mesh processing software.
Guzinski, R., Nieto, H., 2019. Evaluating the feasibility of using Sentinel-2 and Sentinel-3 satellites for high-resolution evapotranspiration estimations. Remote Sens. Environ. 221 (November), 157–172.
Hatfield, J., et al., 2014. Climate Change Impacts in the United States: The Third National Climate Assessment. Agriculture 6, 150–174.
Hatfield, J.L., Dold, C., 2019. Water-use efficiency: advances and challenges in a changing climate. Front. Plant Sci. 0, 103. -103.
Heald, C.L., Spracklen, D.V., 2015. Land use change impacts on air quality and climate. Chem. Rev. 115 (10), 4476–4496.
Heidbach, K., Schmid, H.P., Mauder, M., 2017. Experimental evaluation of flux footprint models. Agric. For. Meteorol. 246 (June), 142–153.
Heinemann, S., et al., 2020. Land surface temperature retrieval for agricultural areas using a novel UAV platform equipped with a thermal infrared and multispectral sensor. Remote Sens. (Basel) 12 (7), 1075. -1075.
Heinzeller, D., et al., 2018. The WASCAL high-resolution regional climate simulation ensemble for West Africa: concept, dissemination and assessment. Earth Syst. Sci. Data 10 (2), 815–835.
Hijmans, R.J. et al., 2021. Package 'raster': geographic Data Analysis and Modeling.
Hoffmann, H., et al., 2016. Crop water stress maps for an entire growing season from visible and thermal UAV imagery. Biogeosciences 13, 6545–6563.
Kelly, J., et al., 2019. Challenges and best practices for deriving temperature data from an uncalibrated UAV thermal infrared camera. Remote Sens. (Basel) 11 (5).
Kim, H.W., Hwang, K., Mu, Q., Lee, S.O., Choi, M., 2012. Validation of MODIS 16 global terrestrial evapotranspiration products in various climates and land cover types in Asia. KSCE J. Civil Eng. 16 (2), 229–238.
Kljun, N., Calanca, P., Rotach, M.W., Schmid, H.P., 2015. A simple two-dimensional parameterisation for Flux Footprint Prediction (FFP). Geosci. Model Dev. 8 (11), 3695–3713.
Knauer, J.J., et al., 2018. Bigleaf-An R package for the calculation of physical and physiological ecosystem properties from eddy covariance data. PLoS ONE 13 (8) e0201114-e0201114.
Kolle, O. and Rebmann, C., 2009. EddySoft: documentation of a software package to acquire and process eddy covariance data.
Kuivanen, K.S., et al., 2016. Characterising the diversity of smallholder farming systems and their constraints and opportunities for innovation: a case study from the Northern Region, Ghana. NJAS - Wageningen J. Life Sci. 78, 153–166.
Kustas, W.P., et al., 2004. Effects of remote sensing pixel resolution on modeled energy flux variability of croplands in Iowa. Remote Sens. Environ. 92 (4), 535–547.
Kuyah, S., et al., 2019. Agroforestry delivers a win-win solution for ecosystem services in sub-Saharan Africa. A meta-analysis. Agronomy Sustain. Dev. 39 (5), 1–18.
Leutner, B., Horning, N., Schwalb-Willmann, J. and Hijmans, R.J., 2019. Package 'RStoolbox': tools for remote sensing data analysis.
Liu, Y., Hiyama, T., Yasunari, T., Tanaka, H., 2012. A nonparametric approach to estimating terrestrial evaporation: validation in eddy covariance sites. Agric. For. Meteorol. 157, 49–59.
Lowder, S.K., Skoet, J., Raney, T., 2016. The number, size, and distribution of farms, smallholder farms, and family farms worldwide. World Dev. 87, 16–29.
Lu, Z., Zhao, Y., Wei, Y., Feng, Q., Xie, J., 2019. Differences among evapotranspiration products affect water resources and ecosystem management in an australian catchment. Remote Sens. (Basel) 11 (8), 958, 2019, Vol. 11, Page 958-958.
Luo, Y., et al., 2020. Nutrients and water availability constrain the seasonality of vegetation activity in a Mediterranean ecosystem. Glob. Chang. Biol. 26 (8), 4379–4400.
Luo, Y., et al., 2018. Using near-infrared-enabled digital repeat photography to track structural and physiological phenology in Mediterranean Tree–Grass Ecosystems. Remote Sens. (Basel) 10 (8), 1293, 2018, Vol. 10, Page 1293-1293.
Mauder, M. and Foken, T., 2011. Documentation and instruction manual of the eddy-covariance software package TK3, pp. 60 -60.
Mauder, M., Foken, T., Cuxart, J., 2020. Surface-energy-balance closure over land: a review. Boundary Layer Meteorol. 177 (2–3), 395–426.
Mauder, M., et al., 2018. Evaluation of energy balance closure adjustment methods by independent evapotranspiration estimates from lysimeters and hydrological simulations. Hydrol. Process. 32 (1), 39–50.
Melendo-Vega, J., et al., 2018. Improving the performance of 3-D radiative transfer model FLIGHT to simulate optical properties of a Tree-Grass Ecosystem. Remote Sens. (Basel) 10 (12), 2061. -2061.
Mendiguren, G., Pilar Martín, M., Nieto, H., Pacheco-Labrador, J., Jurdao, S., 2015. Seasonal variation in grass water content estimated from proximal sensing and MODIS time series in a Mediterranean Fluxnet site. Biogeosciences 12 (18), 5523–5535.
Migliavacca, M., et al., 2017. Plant functional traits and canopy structure control the relationship between photosynthetic CO2 uptake and far-red sun-induced fluorescence in a Mediterranean grassland under different nutrient availability. New Phytol. 214 (3), 1078–1091.
Mokhtari, A., Ahmadi, A., Daccache, A., Drechsler, K., 2021. Actual Evapotranspiration from UAV images: a multi-sensor data fusion approach. Remote Sens. (Basel) 13 (12).
Moncrieff, J., Clement, R., Finnigan, J., Meyers, T., 2004. Averaging, detrending, and filtering of eddy covariance time series. Handbook of Micrometeorology, pp. 7–31.
Moncrieff, J.B., et al., 1997. A system to measure surface fluxes of momentum, sensible heat, water vapour and carbon dioxide. J. Hydrol. (Amst) 188-189 (1–4), 589–611.
Nassar, A., et al., 2022. Using remote sensing to estimate scales of spatial heterogeneity to analyze evapotranspiration modeling in a natural ecosystem. Remote Sens. 14 (2).
Nassar, A., et al., 2021. Assessing daily evapotranspiration methodologies from one-time-of-day sUAS and EC information in the GRAPEX project. Remote Sens. (Basel) 13 (15), 2887.
Nassar, A., et al., 2020. Influence of model grid size on the estimation of surface fluxes using the two source energy balance model and sUAS imagery in vineyards. Remote Sens. (Basel) 12 (3), 342.
Nieto, H., Guzinski, R., Sølvsteen, J. and Graae, P., 2021. pyTSEB: a python Two Source Energy Balance model for estimation of evapotranspiration with remote sensing data - ET4FAO version (v2.1.1). Zenodo.
Nieto, H., et al., 2019. Evaluation of TSEB turbulent fluxes using different methods for the retrieval of soil and canopy component temperatures from UAV thermal and multispectral imagery. Irrig. Sci. 37 (3), 389–406.
Niu, H., Hollenbeck, D., Zhao, T., Wang, D., Chen, Y., 2020. Evapotranspiration estimation with small UAVs in precision agriculture. Sensors (Basel) 20 (22).
Niu, H., Zhao, T., Wei, J., Wang, D., Chen, Y., 2021. Reliable Tree-level evapotranspiration estimation of pomegranate trees using Lysimeter and UAV multispectral imagery. In: 2021 IEEE Conference on Technologies for Sustainability (SusTech), pp. 1–6.
Nocco, M.A., et al., 2019. Combining evapotranspiration and soil apparent electrical conductivity mapping to identify potential precision irrigation benefits. Remote Sens. (Basel) 11 (21), 2460, 2019, Vol. 11, Page 2460-2460.
Norman, J.M., Kustas, W.P., Humes, K.S., 1995. Source approach for estimating soil and vegetation energy fluxes in observations of directional radiometric surface temperature. Agric. For. Meteorol. 77 (3–4), 263–293.
Norman, J.M., Kustas, W.P., Prueger, J.H., Diak, G.R., 2000. Surface flux estimation using radiometric temperature: a dual-temperature-difference method to minimize measurement errors. Water Resour. Res. 36 (8), 2263–2274.
Nouri, H., Beecham, S., Anderson, S., Hassanli, A.M., Kazemi, F., 2015. Remote sensing techniques for predicting evapotranspiration from mixed vegetated surfaces. Urban Water J. 12 (5).
Ogutu, B.O., D'Adamo, F., Dash, J., 2021. Impact of vegetation greening on carbon and water cycle in the African Sahel-Sudano-Guinean region. Glob. Planet Change 202, 103524. -103524.
Ortega-Farías, S., et al., 2016. Estimation of energy balance components over a drip-irrigated olive orchard using thermal and multispectral cameras placed on a helicopter-based unmanned aerial vehicle (UAV). Remote Sens. (Basel) 8 (8).
Osborne, C.P., et al., 2018. Human impacts in African savannas are mediated by plant functional traits. New Phytol. 220 (1), 10–24.
Park, S., 2018. Estimating Plant Water Stress and Evapotranspiration using Very-High-Resolution (VHR) UAV Imagery. The University of Melbourne, Melbourne.
Park, S., et al., 2017. Adaptive estimation of crop water stress in nectarine and peach orchards using high-resolution imagery from an unmanned aerial vehicle (UAV). Remote Sens. (Basel) 9 (8), 828, 2017, Vol. 9, Page 828-828.
Payero, J.O., Tarkalson, D.D., Irmak, S., Davison, D., Petersen, J.L., 2008. Effect of irrigation amounts applied with subsurface drip irrigation on corn evapotranspiration, yield, water use efficiency, and dry matter production in a semiarid climate. Agric. Water Manage. 95 (8), 895–908.
Perez-Priego, O., et al., 2017. Evaluation of eddy covariance latent heat fluxes with independent lysimeter and sapflow estimates in a Mediterranean savannah ecosystem. Agric. For. Meteorol. 236, 87–99.
R Core Team, 2020. R: A Language and Environment for Statistical Computing. Vienna, Austria.
Rebmann, C., et al., 2018. ICOS eddy covariance flux-station site setup: a review. Int. Agrophys. 32 (4), 471–494.
Roussel, J.-R. and Auty, D., 2021. Airborne LiDAR Data Manipulation and Visualization for Forestry Applications.
Rubio, E., Caselles, V., Badenas, C., 1997. Emissivity measurements of several soils and vegetation types in the 8–14, μm Wave band: analysis of two field methods. Remote Sens. Environ. 59 (3), 490–521.
Rufenacht, D., Fredembach, C., Susstrunk, S., 2014. Automatic and accurate shadow detection using near-infrared information. IEEE Trans. Pattern Anal. Mach. Intell. 36 (8), 1672–1678.
Schloerke, B. et al., 2021. GGally: extension to 'ggplot2'.
Schmugge, T., French, A., Ritchie, J.C., Rango, A., Pelgrum, H., 2002. Temperature and emissivity separation from multispectral thermal infrared observations. Remote Sens. Environ. 79 (2), 189–198.

Simpson, J.E., et al., 2021. High spatial and temporal resolution energy flux mapping of different land covers using an off-the-shelf unmanned aerial system. Remote Sens. (Basel) 13 (7), 1286. -1286.
Singh, N., et al., 2021. Climate-driven acceleration in forest evapotranspiration fuelling extreme rainfall events in the Himalaya. Environ. Res. Lett. 16 (8), 084042. -084042.
Sugita, M., Matsuno, A., El-Kilani, R.M.M., Abdel-Fattah, A., Mahmoud, M.A., 2017. Crop evapotranspiration in the Nile Delta under different irrigation methods. Hydrol. Sci. J.-J. Des. Sci. Hydrol. 62 (10), 1618–1635.
Sullivan, R.C., Kotamarthi, V.R., Feng, Y., 2019. Recovering evapotranspiration trends from biased CMIP5 simulations and sensitivity to changing climate over North America. J. Hydrometeorol. 20 (8), 1619–1633.
Susan Morana, M., Humesb, K.S., Pinter Jr., P.J., 1997. The scaling characteristics of remotely-sensed variables sparsely-vegetated heterogeneous landscapes. J. Hydrol. (Amst) 190, 337–362.
Sylla, M.B., Pal, J.S., Faye, A., Dimobe, K., Kunstmann, H., 2018. Climate change to severely impact West African basin scale irrigation in 2 °C and 1.5 °C global warming scenarios. Sci. Rep. 8 (1), 1–9, 2018 8:1.
Torres-Rua, A., 2017. Vicarious calibration of sUAS microbolometer temperature imagery for estimation of radiometric land surface temperature. Sensors 17 (7), 1499. -1499.
UNEP, 2019. Measuring progress. 978-807-3750-9.
United Nations, 2015. Transforming our World: the 2030 Agenda for Sustainable Development.
Wang, D., et al., 2020. A Method of Using WRF-Simulated Surface Temperature to Estimate Daily Evapotranspiration. J. Appl. Meteorol. Climatol. 59 (5), 901–914.
Wheeler, C.E., et al., 2021. A new field protocol for monitoring forest degradation. Front. For. Glob. Change 0, 122. -122.
Wickham, H., 2007. Reshaping Data with the {reshape} Package. J. Stat. Softw. 21 (12), 1–20.
Yang, M., et al., 2020. Assessment of water and nitrogen use efficiencies through UAV-based multispectral phenotyping in winter wheat. Front. Plant. Sci. 11, 927. -927.